iScience

CellPress
OPEN ACCESS

Article

A quinolin-8-ol sub-millimolar inhibitor of UGGT, the ER glycoprotein folding quality control checkpoint

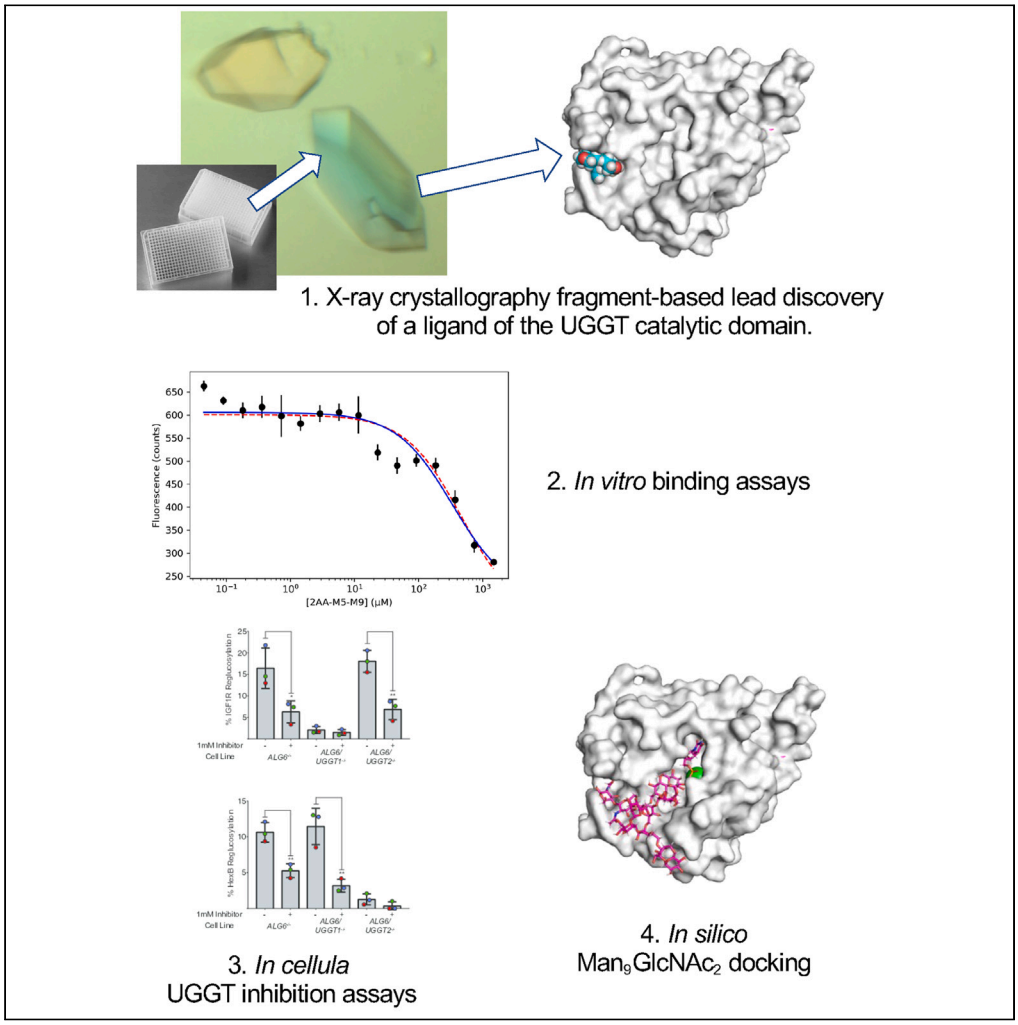

Kevin P. Guay, Roberta Ibba, J.L. Kiappes, ..., Daniel N. Hebert, Nicole Zitzmann, Pietro Roversi

cpmode@gmail.com (C.P.M.)
dhebert@biochem.umass.edu (D.N.H.)
nicole.zitzmann@bioch.ox.ac.uk (N.Z.)
pietro.roversi@cnr.it (P.R.)

Highlights

A ligand of UGGT was discovered by fragment-based lead discovery

The ligand's Kd for a fungal UGGT was measured as 47 μM by ligand-enhanced fluorescence

The ligand inhibits both human UGGT1 and UGGT2 above 750 μM *in cellula*

The ligand and an M5-9 glycan mix compete for overlapping sites on UGGT

Guay et al., iScience *26*, 107919
October 20, 2023
https://doi.org/10.1016/j.isci.2023.107919

iScience

CellPress
OPEN ACCESS

Article

A quinolin-8-ol sub-millimolar inhibitor of UGGT, the ER glycoprotein folding quality control checkpoint

Kevin P. Guay,[1,16] Roberta Ibba,[2,3,16] J.L. Kiappes,[2,16] Snežana Vasiljević,[2] Francesco Bonì,[4] Maria De Benedictis,[5] Ilaria Zeni,[6] James D. Le Cornu,[7] Mario Hensen,[2] Anu V. Chandran,[2] Anastassia L. Kantsadi,[2] Alessandro T. Caputo,[8] Juan I. Blanco Capurro,[9,10] Yusupha Bayo,[11] Johan C. Hill,[2] Kieran Hudson,[12] Andrea Lia,[2,4] Juliane Brun,[2] Stephen G. Withers,[12] Marcelo Martí,[9,10] Emiliano Biasini,[6,13] Angelo Santino,[5] Matteo De Rosa,[4] Mario Milani,[4] Carlos P. Modenutti,[9,10,*] Daniel N. Hebert,[1,*] Nicole Zitzmann,[2,*] and Pietro Roversi[14,15,17,*]

SUMMARY

Misfolded glycoprotein recognition and endoplasmic reticulum (ER) retention are mediated by the ER glycoprotein folding quality control (ERQC) checkpoint enzyme, UDP-glucose glycoprotein glucosyltransferase (UGGT). UGGT modulation is a promising strategy for broad-spectrum antivirals, rescue-of-secretion therapy in rare disease caused by responsive mutations in glycoprotein genes, and many cancers, but to date no selective UGGT inhibitors are known. The small molecule 5-[(morpholin-4-yl)methyl] quinolin-8-ol (5M-8OH-Q) binds a *Ct*UGGT$_{GT24}$ "WY" conserved surface motif conserved across UGGTs but not present in other GT24 family glycosyltransferases. 5M-8OH-Q has a 47 μM binding affinity for *Ct*UGGT$_{GT24}$ *in vitro* as measured by ligand-enhanced fluorescence. *In cellula*, 5M-8OH-Q inhibits both human UGGT isoforms at concentrations higher than 750 μM. 5M-8OH-Q binding to *Ct*UGGT$_{GT24}$ appears to be mutually exclusive to M5-9 glycan binding in an *in vitro* competition experiment. A medicinal program based on 5M-8OH-Q will yield the next generation of UGGT inhibitors.

INTRODUCTION

In the endoplasmic reticulum (ER) of eukaryotic cells, the ER glycoprotein folding quality control (ERQC) system ensures ER retention of immature glycoproteins and assists their folding.[1] Glycoprotein ERQC is central to glycoproteostasis, which in turn plays a major role in health and disease.[2,3] Glycoprotein ERQC is reliant on detection of glycoprotein misfolding, affected by its checkpoint enzyme, UDP-glucose glycoprotein glucosyltransferase (UGGT). UGGT is capable of detecting non-native and slightly misfolded glycoproteins and re-glucosylates its clients to flag them for ER retention.[4,5]

While other components of ERQC have been studied as drug targets,[6–8] cellular consequences of pharmacological modulation of UGGT have been relatively understudied—partly because of the risks associated with targeting core cell housekeeping machineries, and partly because there are no known UGGT selective inhibitors. UGGT is inhibited by its product uridine diphosphate (UDP)[9] and squaryl derivatives

[1]Department of Biochemistry and Molecular Biology, and Program in Molecular and Cellular Biology, University of Massachusetts, Amherst, MA, USA
[2]Oxford Glycobiology Institute, Department of Biochemistry and Kavli Institute for Nanoscience Discovery, South Parks Road, Oxford OX1 3QU, UK
[3]Department of Medicine, Surgery and Pharmacy, University of Sassari, Via Muroni 23A, 07100 Sassari, Italy
[4]Institute of Biophysics, IBF-CNR Unit of Milano, via Celoria 26, 20133 Milano, Italy
[5]Institute of Sciences of Food Production, C.N.R. Unit of Lecce, via Monteroni, 73100 Lecce, Italy
[6]Department of Cellular, Computational and Integrative Biology, University of Trento, Povo, 38123 Trento, Italy
[7]Wellcome Centre for Cell Biology, School of Biological Sciences, University of Edinburgh, Edinburgh, Scotland, United Kingdom
[8]Biomedical Manufacturing, Commonwealth Scientific and Industrial Research Organisation, 343 Royal Parade, Parkville, VIC 3052, Australia
[9]Departamento de Química Biológica, Facultad de Ciencias Exactas y Naturales, Universidad de Buenos Aires, Ciudad Universitaria, Pab. II (CE1428EHA), Buenos Aires, Argentina
[10]Instituto de Química Biológica de la Facultad de Ciencias Exactas y Naturales (IQUIBICEN) CONICET, Ciudad Universitaria, Pab. II (CE1428EHA), Buenos Aires, Argentina
[11]Department of Biosciences, University of Milano, via Celoria 26, 20133 Milano, Italy
[12]Department of Chemistry, University of British Columbia, 2036 Main Mall, Vancouver, BC V6T 1Z1, Canada
[13]Dulbecco Telethon Institute, University of Trento, Povo, 38123 Trento, Italy
[14]Institute of Agricultural Biology and Biotechnology, IBBA-CNR Unit of Milano, via Bassini 15, 20133 Milano, Italy
[15]Leicester Institute of Chemical and Structural Biology and Department of Molecular and Cell Biology, University of Leicester, Henry Wellcome Building, Lancaster Road, LE1 7HR Leicester, UK
[16]These authors contributed equally
[17]Lead contact
*Correspondence: cpmode@gmail.com (C.P.M.), dhebert@biochem.umass.edu (D.N.H.), nicole.zitzmann@bioch.ox.ac.uk (N.Z.), pietro.roversi@cnr.it (P.R.)
https://doi.org/10.1016/j.isci.2023.107919

of UDP[10]; by the non-hydrolyzable UDP-Glucose (UDP-Glc) cofactor analog UDP-2-deoxy-2-fluoro-D-glucose (U2F); and by synthetic analogs of the *N*-linked $Man_9GlcNAc_2$ glycan substrate,[11,12] but obviously none of these molecules are UGGT specific. Selective and potent UGGT modulators would be important reagents for interrogating the cell biology of the secretory pathway, as well as having therapeutic potential in several areas of medical science (such as virology,[13–15] metabolic and rare genetic disease,[16–18] immunology,[5] and cancer[19–21]), biotechnology, and agricultural science.[22–25]

We set out to search for ligands of UGGT by fragment-based lead discovery (FBLD) using X-ray crystallography, an approach which requires the growth of hundreds of well-diffracting crystals of the target.[26–29] No crystal structures of mammalian UGGTs have been obtained so far, but atomic resolution structures of UGGTs from thermophilic fungi have been determined.[30–32] None of the crystals of full-length UGGT we grew so far diffracted past 2.8 Å,[30,32] but 1.35 and 1.4 Å crystal structures of the catalytic domain of *Thermomyces dupontii* UGGT (*Td*$UGGT_{GT24}$), in complex with UDP and UDP-Glc, respectively, have been described.[31] Although compounds binding the UGGT N-terminal folding-sensor domains of the enzyme would also be potential UGGT inhibitors, we decided to target the UGGT C-terminal catalytic domain (belonging to the GlycosylTransferase Family 24 (GT24) fold), given the high 70% similarity and 60% identity between human and fungal sequences in this portion of the enzyme.

Toward the FBLD of ligands of the UGGT C-terminal catalytic domain, we cloned in the pHLsec vector for secreted mammalian expression[33] the catalytic domain of *Chaetomium thermophilum* UGGT (*Ct*$UGGT_{GT24}$), without its C-terminal ER-retrieval motif, and expressed, purified, and crystallized the protein.[34] We then used those *Ct*$UGGT_{GT24}$ crystals for our FBLD effort, in which each crystal was soaked with a different chemical compound from a molecular fragment library.[34] The study's best hit was a 2.25 Å crystal structure of *Ct*$UGGT_{GT24}$ in complex with the fragment ligand 5-[(morpholin-4-yl)methyl]quinolin-8-ol, 5M-8OH-Q for short in what follows.

Here, we describe the 1.65 Å structure of a co-crystal of *Ct*$UGGT_{GT24}$ and 5M-8OH-Q ($^{5M-8OH-Q}$*Ct*$UGGT_{GT24}$), as well as the crystal structures of apo *Ct*$UGGT_{GT24}$ and *Ct*$UGGT_{GT24}$ in complex with the U2F cofactor analog (^{U2F}*Ct*$UGGT_{GT24}$). We measure the 5M-8OH-Q affinity for *Ct*$UGGT_{GT24}$ and human UGGT1 *in vitro* and show that in human cells the molecule inhibits both human paralogs of UGGT, UGGT1, and UGGT2, at concentrations higher than 750 μM. We present an *in silico* model of the $GlcNac_2Man_9$ *N*-linked glycan in the catalytic site of UGGT, suggesting that the ligand interferes with N-glycan binding, therefore likely acting as a competitive inhibitor. This hypothesis is supported by a competition assay *in vitro*, in which the *N*-linked glycan displaces the inhibitor from its binding site in the UGGT catalytic domain. A medicinal chemistry program to generate more potent and selective UGGT inhibitors starting from 5M-8OH-Q is in progress.

RESULTS

The active site of *Ct*$UGGT_{GT24}$ undergoes structural rearrangements upon binding the U2F cofactor analog

The crystal structures of *Ct*$UGGT_{GT24}$ in absence of the UDP-Glc cofactor and of the same protein in complex with the U2F cofactor analog (^{U2F}*Ct*$UGGT_{GT24}$) were determined by X-ray crystallography. Tables S1 and S2 list the X-ray data collection statistics and structure refinement statistics, respectively. These structures constituted the basis for the FBLD effort that discovered 5M-8OH-Q as a *Ct*$UGGT_{GT24}$ ligand.[34]

The *Ct*$UGGT_{GT24}$ active site undergoes structural changes binding the U2F cofactor analog. Half of the coordination sphere of the Ca^{2+} ion in the *Ct*$UGGT_{GT24}$ active site is common to both structures: the side chains of D1302 and D1304 (belonging to the UGGT conserved DAD motif[35]) and the side chain of the conserved D1435 always take up three invariant coordination sites around the Ca^{2+} ion (Figures 1A and 1B). In the 1.8 Å structure of apo *Ct*$UGGT_{GT24}$ (PDB ID 7ZKC), two water molecules occupy two of the three remaining coordination sites around the Ca^{2+} ion, with the main chain carbonyl oxygen of L1436 completing the ion's octahedral coordination (Figure 1A). In the ^{U2F}*Ct*$UGGT_{GT24}$ structure (PDB ID 7ZLU) these two water molecules are replaced by an O atom from the β phosphate and by the F atom on the Glc ring of U2F (Figure 2A); the main chain of L1436 moves away from the Ca^{2+} ion, and a water molecule occupies its Ca^{2+} coordination site (Figures 1B, 1C, and 2A).

In the *Ct*$UGGT_{GT24}$ binding site, U2F adopts a conformation equivalent to that of UDP-Glc described in Caputo et al.[34] This conformation likely represents the initial stage of the cofactor binding process: the ribose ring points toward the solvent (Figures 1B and 1C and 2A). The uracyl ring O4 atom accepts a hydrogen bond from the main chain NH of S1207, and its N3 atom donates one hydrogen bond to the main chain O of the same residue (Figures 1B and 1C); the uracyl ring also forms a π-stacking interaction with the conserved *Ct*UGGT Y1211, whose side chain rotates slightly when compared to the apo structure, to accommodate the ligand. The molecule's pose suggests that the UGGT active site selects UDP-Glc over UDP-Gal[36–39]: in UDP-Glc the glucose O4′ atom forms hydrogen bonds to the side chains of conserved W1280 and D1396, but these interactions would be lost in UDP-Gal, because of the difference in stereochemistry between Glc and Gal in position 4 (Figure 1C).

UGGT binds 5M-8OH-Q via a conserved patch on the surface of its catalytic domain

To confirm the 5M-8OH-Q:*Ct*$UGGT_{GT24}$ binding pose observed in the FBLD soaked crystal,[34] we grew a *Ct*$UGGT_{GT24}$:5M-8OH-Q co-crystal and obtained a 1.65 Å crystal structure ($^{5M-8OH-Q}$*Ct*$UGGT_{GT24}$, PDB ID 7ZLL). The structure confirms that the compound binds to a conserved patch on the surface of the *Ct*$UGGT_{GT24}$ domain, about 15 Å away from the UDP-Glc binding site (Figures 1D, S1A, and S1B). The morpholine ring is partially disordered in the crystal, but one of its ring placements is 4.2 Å from the conserved ^{1396}DQD^{1398} motif coordinating the Glc ring of UDP-Glc or U2F (Figures 1D and 2A); the ligand also causes a displacement of the side chain of *Ct*$UGGT_{GT24}$ ^{1346}Y.[34] Through this displacement, the 8OH-quinoline ring inserts and is sandwiched between the aromatic side chains of the conserved residues ^{1346}YW^{1347}—which we propose to call the "YW clamp". The two aromatic side chains stabilize the quinoline ring forming an aromatic trimer[41]; the 8OH group of the quinoline also establishes a hydrogen bond to the side chain of ^{1402}H (Figures 1D and S1B).

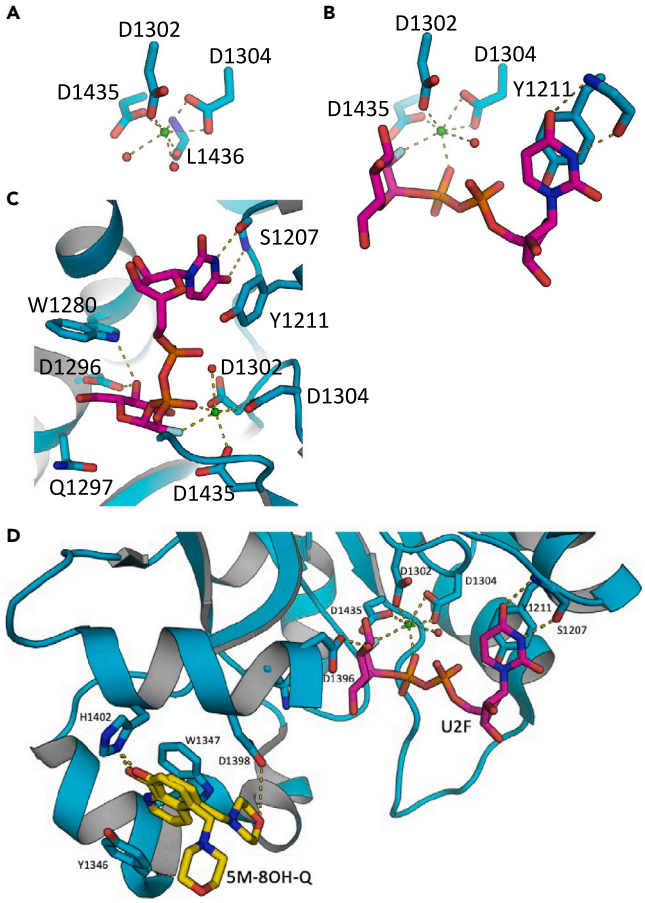

Figure 1. *Ct*UGGT$_{GT24}$ crystal structures

(A–C) The active sites of *Ct*UGGT$_{GT24}$ and ^{U2F}*Ct*UGGT$_{GT24}$. Protein atoms in sticks representation; C cyan (but U2F C magenta, and 5M-8OH-Q C atoms yellow), O red, N blue, P orange, F light green. H-bonds and Ca^{2+}-coordination bonds are in yellow dashed lines. The Ca^{2+} ion is a green sphere and its coordinating water molecules are red spheres. The side chains of residues D1302, D1304, and D1435 coordinate the Ca^{2+}. (A) apo *Ct*UGGT$_{GT24}$ (PDB ID 7ZKC). The octahedral coordination sphere of the Ca^{2+} ion is completed by two water molecules and the main chain of L1436. (B) ^{U2F}*Ct*UGGT$_{GT24}$ (PDB ID 7ZLU). L1436 moves away from the Ca^{2+} ion, and two coordination sites are taken up by the U2F β phosphate and the F atom at position 2′ of the Glc ring. The uracyl O4 atom accepts an H-bond from the S1207 main chain NH. Only one Ca^{2+}-coordinating water molecule remains. (C) the UGGT active site selects UDP-Glc over UDP-Gal[36–39]: in UDP-Glc the glucose O4′ atom forms hydrogen bonds to the side chains of conserved W1280 and D1396, but these interactions would be lost in UDP-Gal (because of the difference in stereochemistry between Glc and Gal in position 4). The side chain of Y1211 and the main chain of S1207 coordinate the uracyl ring.

(D) The ^{U2F}*Ct*UGGT$_{GT24}$ structure (PDB ID 7ZLU) overlaid with the 5M-8OH-Q ligand from the $^{5M-8OH-Q}$*Ct*UGGT$_{GT24}$ structure (PDB ID 7ZLL), in the enzyme active site region. The *Ct*UGGT ^{1346}YW^{1347} clamp, the conserved ^{1346}DQD^{1347} motif, H1402, Y1211, and the main chain of S1207 are in stick representation. Only two of the many poses of the 5M-8OH-Q inhibitor are shown.

5M-8OH-Q and M9 glycan-binding sites overlap

To gain insight into how 5M-8OH-Q UGGT binding compares with UGGT substrate binding, we built an *in silico* model of the Man$_9$GlcNAc$_2$ glycan bound to *Ct*UGGT using a combination of knowledge-based docking and molecular dynamics (see STAR Methods).

The surface of the UGGT catalytic domain on which the glycan docks according to our model is highly conserved across eukaryotic UGGT1s and UGGT2s.[42] The A branch of the Man$_9$GlcNAc$_2$ glycan stretches toward the UGGT active site, while B and C branches point toward the solvent, fitting into shallower grooves, binding the protein with fewer interactions (Figure 2B). These observations are consistent with previous work showing that UGGT is able to glucosylate misfolded glycoproteins bearing GlcNAc$_2$Man$_8$ (Man "I" trimmed) and GlcNAc$_2$Man$_7$ (Man "I" and Man "K" trimmed) glycans (Figure 2B) albeit with lower efficiency than those bearing GlcNAc$_2$Man$_9$.[43]

Importantly, the model suggests how UGGT recognizes the first GlcNAc: the glycan's first *N*-acetamide group faces directly into the hydrophobic cavity formed by residues Y1346, W1347, and L1392, its acetyl oxygen hydrogen-bonded to the L1392 backbone nitrogen, and the S1391 hydroxyl group (Figures 2C and 2D), in agreement with the published finding that the first GlcNAc is required for the Man$_9$GlcNAc$_2$ glycan to bind to UGGT.[43,44]

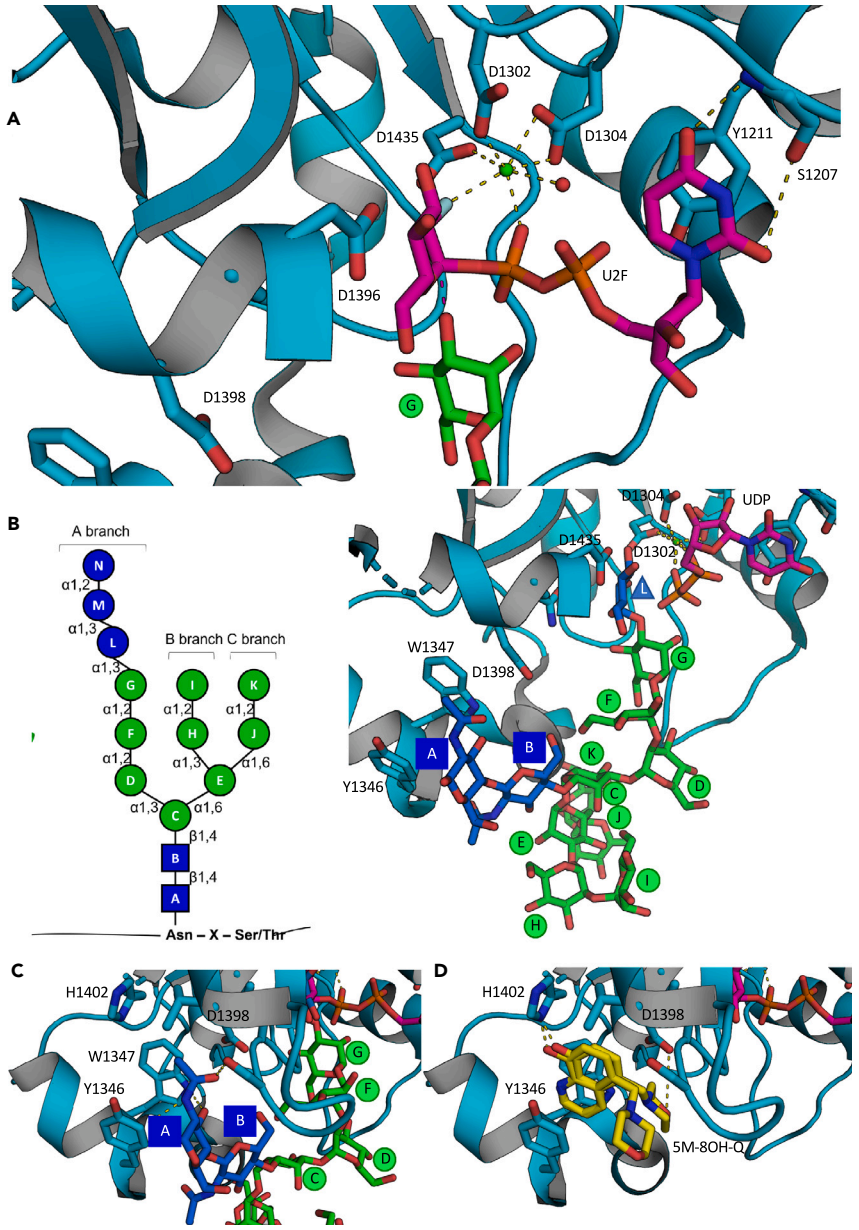

Figure 2. Modeling of the $GlcNAc_2Man_9$ glycan bound to the *Ct*$UGGT_{GT24}$ domain

(A) Man "G" placement next to the UDP-Glc binding site, in an orientation suitable for the nucleophilic attack of its O3 oxygen to the glucose anomeric center (red dashed line), to yield the β(1–3) Glc-Man bond.

(B) $GlcNAc_2Man_9Glc_3$ glycan nomenclature and final model of the $GlcNAc_2Man_9Glc_1$ glycan docked onto the *Ct*$UGGT_{GT24}$ domain. Saccharide moieties are color-coded according to the scheme on the left hand side.[40]

(C and D) The docked $GlcNAc_2$ moiety of the $Man_9GlcNAc_2$ *N*-linked glycan and 8-OH-Q share a binding pocket.

To test the hypothesis that 5M-8OH-Q and the *N*-linked glycan of a client glycoprotein compete for overlapping sites, we set up assays *in vitro*. Initially, the affinity of 5M-8OH-Q for full-length human UGGT1 (UGGT1) was measured by saturation transfer difference (STD) Nuclear Magnetic Resonance (NMR) spectroscopy, but no signal was measurable below 100 μM 5M-8OH-Q concentration, and a weak binding event with a 613 μM K_d was measured—the significance of which remains unclear (Figure S3A). For the remaining binding assays, we decided to exploit detection of fluorescence, from either of two kinds of fluorescently labeled molecules: 2-anthranylic acid-labeled *N*-linked glycans (2AA-glycans, Figure 3A) or N-NHS-RED-labeled *Ct*$UGGT_{GT24}$ protein (Figure 3B).

Fluorescence from 2-anthranylic acid-labeled $GlcNAc_2Man_9$ glycan (2AA-M9) was used as the basis of detection only in one experiment, in which we followed its binding to the *Ct*$UGGT_{GT24}$ domain *in vitro* (Figure S4A) using fluorescence polarization anisotropy (FPA). The

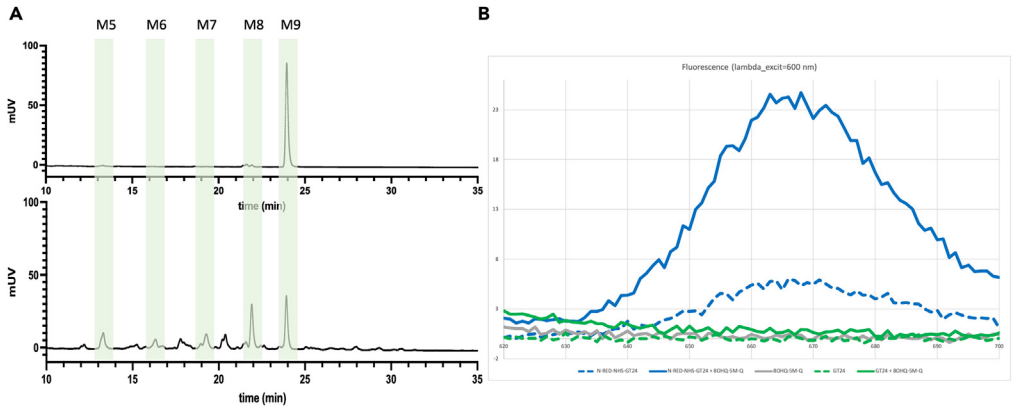

Figure 3. Fluorescence from 2AA-labeled glycans and N-NHS-RED-labeled *Ct*UGGT$_{GT24}$

(A) HPLC elution profiles for the purification of 2AA-labeled glycans obtained from recombinantly expressed HIV gp120. Top panel, black trace: 2AA-labeled glycans purified from cells treated with 10 μM kifunensine (predominantly $GlcNAc_2Man_9$, i.e., 2AA-M9 glycan). Bottom panel: 2AA-labeled glycans purified from cells not treated with kifunensine: mostly 2AA-M9 glycan, but containing 2AA-M5, 2AA-M6, 2AA-M7 and 2AA-M8 glycans as well. We call this mixture 2AA-M5-9.

(B) Fluorescence spectra of 5M-8OH-Q, unlabelled *Ct*UGGT$_{GT24}$ and NT-RED-NHS-labeled *Ct*UGGT$_{GT24}$. λ_{Excit} = 600 nm. Solid and dashed lines refer to samples with or without 5M-8OH-Q, respectively. Gray: 5M-8OH-Q 2.5 mM; green dashed: unlabelled *Ct*UGGT$_{GT24}$ 1.7 μM; green: unlabelled *Ct*UGGT$_{GT24}$ 1.7 μM plus 5M-8OH-Q 2.5 mM; blue dashed: NT-RED-NHS-labeled *Ct*UGGT$_{GT24}$ 1.7 μM; blue: NT-RED-NHS-labeled *Ct*UGGT$_{GT24}$ 1.7 μM plus 5M-8OH-Q 2.5 mM.

FPA-estimated dissociation constant for the binding of *Ct*UGGT$_{GT24}$ to the 2AA-M9 *N*-linked glycan is K_d = 117 ± 32 μM. No measurement of the affinity of UGGT for an *N*-linked glycan has been published before, although a Michaelis Menten K_m = 18 μM was reported for misfolded soybean agglutinin and bovine thyroglobulin in reglucosylation assays mediated by full-length rat UGGT.[35]

The remaining *in vitro* binding assays followed fluorescence from N-NHS-RED-labeled *Ct*UGGT$_{GT24}$ protein. This signal was preliminarly characterized by acquisition of fluorescence spectra in the 620–700 nm range, using λ_{excit} = 600 nm ((Figure 3B)). Fluorescence spectra from solutions containing either 5M-8OH-Q or *Ct*UGGT$_{GT24}$ (with or without N-NHS-RED-labeling), or both, were measured. No fluorescence was detected from 5M-8OH-Q (gray fluorescence spectrum in Figure 3B), nor from unlabeled *Ct*UGGT$_{GT24}$ protein, with or without 5M-8OH-Q (green fluorescence spectra in Figure 3B). N-NHS-RED-labeled *Ct*UGGT$_{GT24}$ fluoresced at a low level (dashed blue spectrum in Figure 3B). Addition of 5M-8OH-Q to N-NHS-RED-labeled *Ct*UGGT$_{GT24}$ appeared to enhance its fluorescence 5-fold (solid blue spectrum in Figure 3B).[45] Since no difference in fluorescence was observed from SDS/heat-denatured N-NHS-RED-labeled *Ct*UGGT$_{GT24}$ protein with or without 5M-8OH-Q (data not shown), it appears that the observed 5M-8OH-Q-induced enhancement of N-NHS-RED-labeled *Ct*UGGT$_{GT24}$ fluorescence depends on binding of 5M-8OH-Q to the labeled *Ct*UGGT$_{GT24}$ in its native structure/fold (ligand-enhanced fluorescence, LEF).[46]

Three *in vitro* experiments followed binding of ligands to N-NHS-RED-*Ct*UGGT$_{GT24}$, either by LEF or by microscale thermophoresis (MST). Those are as follows.

1. Binding of N-NHS-RED-*Ct*UGGT$_{GT24}$ to 5M-8OH-Q was assayed by measuring LEF of a fixed amount of NHS-RED-*Ct*UGGT$_{GT24}$ along a dilution series of 5M-8OH-Q (Figure S3B). The equilibrium dissociation constant of the N-NHS-RED-*Ct*UGGT$_{GT24}$:5M-8OH-Q complex is estimated as $K_d^{5M-8OH-Q}$ = 47 ± 0.7 μM.
2. Binding of a mixture of 2AA-$GlcNAc_2Man_{5-9}$ glycans (2AA-M5-9) to N-NHS-RED-labeled *Ct*UGGT$_{GT24}$ was measured using MST (Figure S4B). The average affinity of N-NHS-RED-labeled *Ct*UGGT$_{GT24}$ for the 2AA-M5-9 *N*-linked glycan mixture is $K_d^{2AA-M5-9}$ = 250 ± 39 μM, weaker than the K_d^{2AA-M9} = 117 ± 32 μM we measured by FPA between *Ct*UGGT$_{GT24}$ and the 2AA-M9 *N*-linked glycan (Figure S4). These values are consistent with the loss of protein affinity expected for *N*-linked glycan species with fewer than 9 mannose residues.
3. Binding of the 2AA-M5-9 mixture to *Ct*UGGT$_{GT24}$ in presence of 40 μM 5M-8OH-Q was assayed in an *in vitro* competition experiment. The changes of fluorescence of the 5M-8OH-Q:N-NHS-RED-labeled *Ct*UGGT$_{GT24}$ complex were followed along a 2AA-M5-9 dilution series (black data points in Figure 4). The same changes in fluorescence were then computed with a model in which two simultaneous equilibria are established, but no ternary complex can form; i.e., 5M-8OH-Q and 2AA-M5-9 *N*-linked glycan binding to N-NHS-RED-labeled *Ct*UGGT$_{GT24}$ are mutuallfy exclusive. The calculation used the two K_ds measured in the experiments described earlier: $K_d^{5M-8OH-Q}$ = 47 ± 0.7 μM and $K_d^{2AA-M5-9}$ = 250 ± 39 μM. The main qualitative trend of the 2AA-M5-9-induced displacement of 5M-8OH-Q from N-NHS-RED-labeled *Ct*UGGT$_{GT24}$ is well predicted by this model (red curve in Figure 4), suggesting that 5M-8OH-Q and the 2AA-M5-9 glycans compete for overlapping sites. A fit to the same data using a model with a single equilibrium gives an apparent dissociation constant of $^{app}K_d^{2AA-M5-9}$ = 341 μM (blue dashed curve in Figure 4).

5M-8OH-Q is a sub-millimolar inhibitor of human UGGTs *in cellula*

To ascertain if 5M-8OH-Q can be delivered to the ER and inhibit UGGT-mediated glucosylation *in cellula*, modified HEK293-6E cells were treated with the inhibitor, monoglucosylated glycoproteins isolated by affinity precipitation (with a glutathione S-transferase

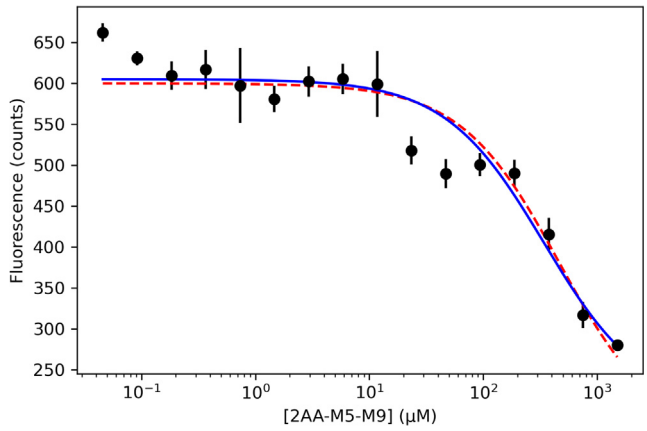

Figure 4. 5M-8OH-Q and the 2AA-M5-9 *N*-linked glycan mixture compete for N-NHS-RED-labeled *Ct*UGGT$_{GT24}$ *in vitro*

Black filled circles: 2AA-M5-9 *N*-linked glycan dilution series from 1.5 mM to 45.8 nM, displacing 40 μM 5M-8OH-Q from 100 nM NT-RED-NHS-labeled *Ct*UGGT$_{GT24}$, as measured by LEF. λ_{Excit} = 650 nm λ_{Emiss} = 670 nm. Error bars are esds from four independent dilution series. Red dashed line: calculated fluorescence from NT-RED-NHS-labeled *Ct*UGGT$_{GT24}$ in the above conditions, using two mutually exclusive binding equilibria and the two measured $K_d^{5M-8OH-Q}$ = 47 μM and $K_d^{2AA-M5-9}$ = 250 μM. Blue line: a fit to the data using a model with a single equilibrium gives $^{app}K_d^{2AA-M5-9}$ = 341 μM.

[GST]-calreticulin [GST-CRT] resin), and the eluate analyzed by immunoblotting.[47,48] To ensure the CRT interaction resulted from UGGT glucosylation, and not from the initial glycan trimming that occurs during normal glycan maturation, CRISPR/Cas9 was used to knock out the alpha-1,3-glucosyltransferase 6 (*ALG6*) gene. ALG6 appends the first glucose to the $Man_9GlcNAc_2$ carbohydrate during the synthesis of the $Glc_3Man_9GlcNAc_2$ *N*-linked glycan precursor at the ER membrane. Once the ALG-mediated synthesis of its precursor is complete, the $Glc_3Man_9GlcNAc_2$ glycan is then appended to nascent glycoproteins by Oligosaccharyl Transferase (OST) and trimmed by glucosidases I and II to a monoglucosylated state, which in turn can bind to the ER lectin chaperones calnexin and calreticulin.[49] Therefore, during glycan maturation in wild-type cells, CRT-affinity pull-downs would select two types of glycoproteins: either those with a glycan trimmed from Glc_3 $Man_9GlcNAc_2$ to $GlcMan_9GlcNAc_2$ or those which underwent glucosylation of a $Man_9GlcNAc_2$ glycan by a UGGT.[50] In our *ALG6*$^{-/-}$cells, the CRT-affinity pull-down can only select monoglucosylated glycoproteins that were glucosylated by UGGT and not the ones produced by the ER glucosidases initial glycan trimming because in these cells the *N*-glycan precursors added to nascent glycoproteins initially lack the three glucoses.

In order to decide on the maximum assay concentration of 5M-8OH-Q, toxicity assays were carried out. In a trypan blue assay, toxic effects were observed around 1–2 mM 5M-8OH-Q and above in modified HEK293-6E cells: after 5 h of treatment with 1 or 2 mM 5M-8OH-Q the viability was about 75%–80% (Figure S5).

The *ALG6*$^{-/-}$ HEK293-6E cells were treated with increasing concentrations of 5M-8OH-Q, and—following incubation with the molecule—glucosylation of known UGGT substrate glycoproteins was analyzed by isolating monoglucosylated glycoproteins from the cell lysate. After GST-CRT precipitation, the eluate was probed for two known substrates of UGGT: the proprotein of human insulin like growth factor 1 receptor (IGF1R) (ProIGF1R, a UGGT1 substrate[48]) and the proprotein of hexosaminidase subunit beta (HexB) (ProHexB, a UGGT2 substrate[48]), and their glucosylation levels were quantified. The amount quantified in each GST-CRT pull-down was divided by the total amount found within the sample's whole-cell lysate (WCL), resulting in the percent glucosylation at that dose of 5M-8OH-Q.[48]

Levels of monoglucosylated IGF1R and HexB in the *ALG6*$^{-/-}$ HEK293-6E cells decrease as the concentration of 5M-8OH-Q increases (Figure 5A, even-numbered lanes 2–18). In particular, a significant decrease in IGF1R and HexB glucosylation is observed at 500 and 750 μM 5M-8OH-Q, respectively. IGF1R and HexB glucosylation decreases from ~ 17% to ~ 4% and ~ 9% to ~ 2%, respectively, going from no treatment to 2 mM 5M-8OH-Q (Figures 5B–5D).

Interestingly, the overall levels of IGF1R and HexB glycoproteins also seem to decrease with increasing levels of 5M-8OH-Q (WCL lanes in Figure 5A).

Next, we asked whether 5M-8OH-Q inhibits both human paralogs of UGGT (UGGT1 and UGGT2).[48,51,52] *ALG6/UGGT1*$^{-/-}$ and *ALG6/UGGT2*$^{-/-}$ double knockout (KO) cells[48] were exposed to 1 mM of the drug to measure glucosylation of IGF1R and HexB as described earlier (Figure 6A). As expected, glucosylation of IGF1R (a UGGT1 substrate[48]) is significantly inhibited in both the *ALG6*$^{-/-}$ and *ALG6/UGGT2*$^{-/-}$ cells, but not in the *ALG6/UGGT1*$^{-/-}$ cell line (Figure 6B). Similarly, glucosylation of the UGGT2 substrate HexB is inhibited in the *ALG6*$^{-/-}$ and *ALG6/UGGT1*$^{-/-}$ cells, but not in the *ALG6/UGGT2*$^{-/-}$ cell line (Figure 6C). The levels of inhibition within each of these UGGT KO cell lines agree well with the findings described earlier (Figure 5; Adams et al.[48]). In agreement to what is observed in Figure 5A, 5M-8OH-Q also decreases the levels of IGF1R and HexB in the WCL lanes (Figure 6A). Taken together these results suggest 5M-8OH-Q can reach the ER and inhibit both paralogs of UGGT.

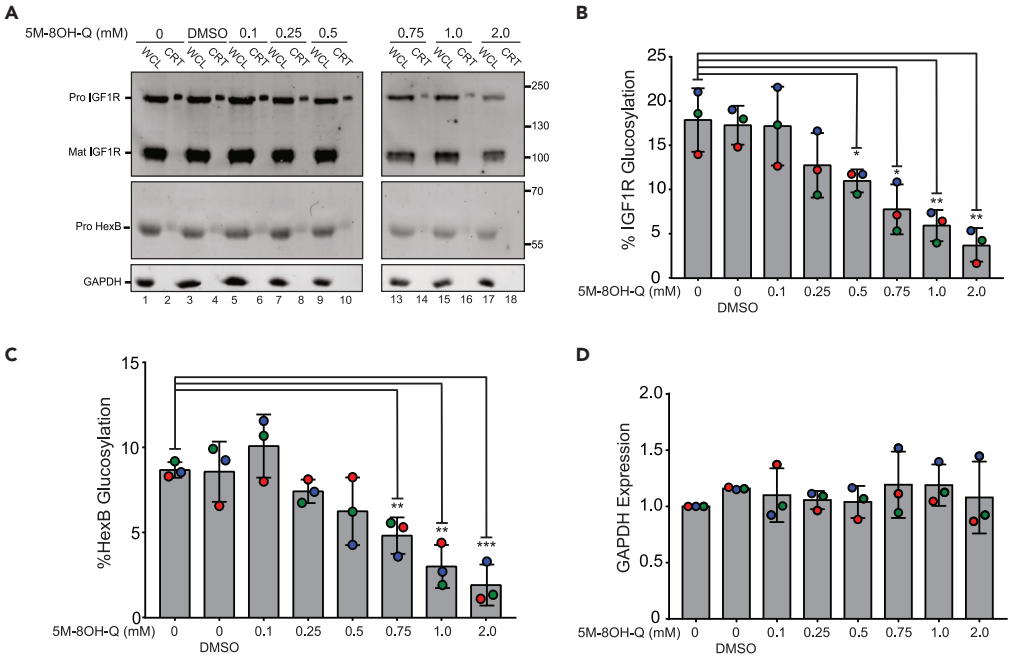

Figure 5. 5M-8OH-Q dose-dependent inhibition of UGGT *in cellula*

(A) *ALG6*$^{-/-}$ HEK293-6E cells were cultured and treated with increasing concentrations of 5M-8OH-Q. The "0 mM" group was treated with no drug or vehicle. The vehicle control group was incubated with DMSO. The lysate was split between a whole-cell lysate sample (20%, "WCL") and a GST-CRT pull-down sample (60%, "CRT"), and resolved by 9% SDS-PAGE gel electrophoresis, before transferring the protein bands to a PVDF membrane. Imaged are immunoblots probed for IGF1R (whose proprotein *Hs*ProIGF1R is a UGGT1 substrate[48]), HexB (whose proprotein *Hs*ProHexB is a UGGT2 substrate[48]) and GAPDH (loading control). Each data point comes from three independent biological replicates.

(B and C) Quantification of *Hs*ProIGF1R and *Hs*ProHexB glucosylation over increasing amounts of 5M-8OH-Q from the experiments in A. Percent glucosylation was calculated by dividing the normalized CRT value by the normalized value from the WCL and multiplying by 100.

(D) Anti-GAPDH blot control. Protein samples were loaded to match the protein in the "0 mM" group for each condition. Error bars represent the standard deviation. Statistical significance levels: *: $p \leq 0.05$; **: $p \leq 0.01$; ***: $p \leq 0.001$.

DISCUSSION

Since its discovery in 1989,[53] UGGT retains a central role in the standard model of glycoprotein ERQC.[4] As such, and considering the importance of glycoprotein folding to health and disease,[3] UGGT is a potential target for drugs to treat a variety of conditions.[16,20,54] As of today, the only known UGGT inhibitors are its product, UDP,[55] and some of its squaryl derivatives[10]; the UDP-Glc analog U2F; and synthetic analogs of its substrate (the *N*-linked $Man_9GlcNAc_2$ glycan).[11,12] None of these molecules are good scaffolds for selective drug design, given that all eukaryotic genomes encode a plethora of proteins carrying a UDP-, a UDP-Glc-, or a glycan-binding site. Until the molecular mechanisms underpinning misfold recognition are elucidated, and the portions of UGGT involved in this process are discovered,[32] the catalytic domain remains the most promising target for novel classes of compounds that inhibit UGGT-mediated glucosylation of misfolded glycoproteins in the ER.

We grew crystals of $CtUGGT_{GT24}$ in order to hunt for novel ligands by FBLD and discovered 5M-8OH-Q as a $CtUGGT_{GT24}$ ligand.[34] The molecule was originally synthesized as a component for soluble aluminum complex dyes[56] or fluorescent Zinc sensors.[57] In the medical field, 8-hydroxyquinoline derivatives can be used as insecticides, antibacterial, fungicidal, neuroprotective, and anti-HIV agents.[58,59] The 5M-8OH-Q K_d for severe acute respiratory syndrome coronavirus 2 (SARS-CoV-2) main viral protease was estimated as 28.6×10^{-6} M by a recent *in silico* study.[60]

The $^{5M-8OH-Q}CtUGGT_{GT24}$ crystal structure shows that 5M-8OH-Q binds a conserved pocket on the surface of the protein, not far from the UDP-Glc binding site (Figures 1 and 2). *In vitro*, 5M-8OH-Q binds to $CtUGGT_{GT24}$ with 47 μM K_d (Figure S3B). 5M-8OH-Q and M5-9 glycan binding appear to be mutually exclusive in an *in vitro* competition assay (Figure 4). These observations are consistent with the *in silico* model of the $Man_9GlcNAc_2$ glycan bound to the catalytic domain of *Ct*UGGT which shows the 5M-8OH-Q binding site partially overlapping with the putative $Man_9GlcNAc_2$ glycan-binding site.

Our experiments in human cells show a concentration-dependent decrease in glucosylation of the *Hs*ProIGF1R and *Hs*ProHexB UGGT substrates upon treatment of HEK293-6E cells with 5M-8OH-Q (Figure 5), indicating that the molecule inhibits ER lumenal UGGTs. Both UGGT isoforms are inhibited (Figure 6), a result that agrees with the sequence and structure conservation of the 5M-8OH-Q binding site in the catalytic domain of the two proteins.[42]

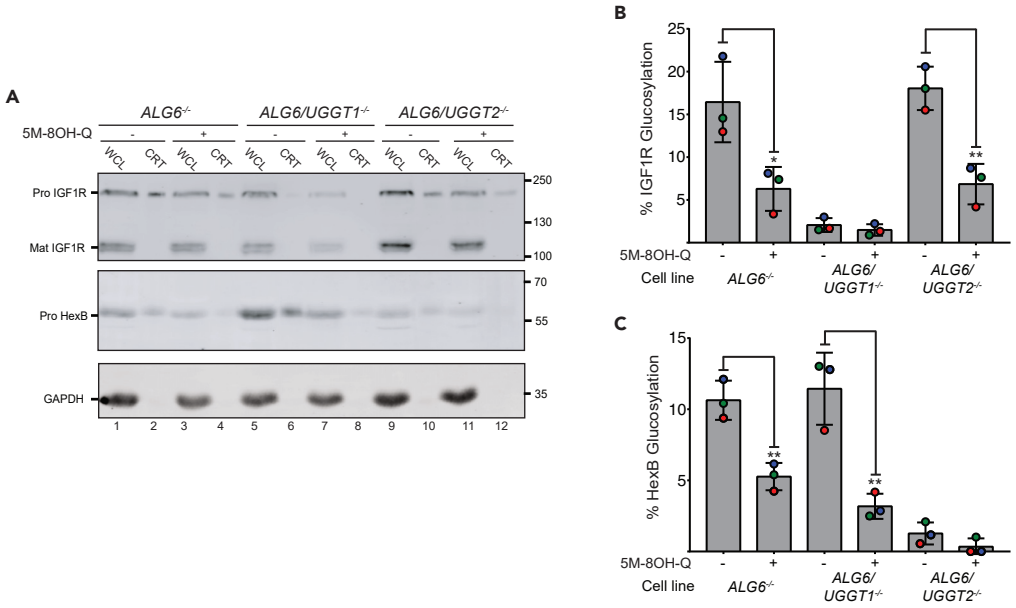

Figure 6. 5M-8OH-Q inhibits both UGGT1 and UGGT2 *in cellula*

(A) *ALG6*$^{-/-}$, *ALG6/UGGT1*$^{-/-}$ and *ALG6/UGGT2*$^{-/-}$ HEK293-6E cells were cultured and either not treated or treated with 1 mM 5M-8OH-Q to determine if the drug inhibits one or both of UGGT1 and UGGT2. After the cells were incubated with the inhibitor, they were lysed and split between a whole-cell lysate sample (20%, "WCL") and a GST-CRT pull-down sample (60%, "CRT"), and resolved by 9% SDS-PAGE gel electrophoresis, before transferring the protein bands to a PVDF membrane. Imaged are immunoblots probed for IGF1R (UGGT1 substrate[48]) and HexB (UGGT2 substrate[48]). Glucosylation of human ProIGF1R and human ProHexB was observed in *ALG6*$^{-/-}$, *ALG6/UGGT2*$^{-/-}$, and *ALG6*$^{-/-}$, *ALG6/UGGT1*$^{-/-}$ cell lines, respectively. Each data point represents three independent biological replicates. GAPDH was used as a loading control.

(B and C) Quantification of human ProIGF1R and human ProHexB glucosylation from (A) Percent glucosylation was calculated by dividing the normalized value from the CRT lane by the normalized WCL. The resulting value was multiplied by 100 to obtain percent glucosylation. Error bars represent the standard deviation. Statistical significance levels: *: $p \leq 0.05$; **: $p \leq 0.01$; ***: $p \leq 0.001$.

Besides *Hs*UGGT1 and *Hs*UGGT2, the human genome encodes 10 more genes containing a GlycosylTransferase-A (GT-A) or a GlycosylTransferase-B (GT-B) domain. From sequence alignment, it appears that the YW clamp providing the 5M-8OH-Q binding platform is specific to UGGTs (GT24 family[61]; Figure S2). It is therefore unlikely that 5M-8OH-Q binds other GT-A and GT-B domains in human proteins in the same way it binds UGGTs.

Rather, 8OH-quinolines can chelate a great number of cations, including Cu^{2+}, Bi^{2+}, Mn^{2+}, Mg^{2+}, Fe^{3+}, Al^{3+}, Zn^{2+}, and Ni^{3+},[62] and are known to bind to a dozen mammalian metalloproteins (see Table S3), including human demethylases, 2-oxoglutarate/iron-dependent oxygenases, and α-ketoglutarate-dependent RNA demethylases.[63–65] Metalloproteins[66–72] are therefore more likely candidates for any 5M-8OH-Q off-target effects.

In summary, 5M-8OH-Q provides a useful starting point for the synthesis of UGGT modulators for the treatment of diseases caused by "responsive mutants", as persistent UGGT-mediated glucosylation may prevent trafficking of slightly misfolded, but otherwise functional, glycoproteins to their correct cellular locations.[16] UGGT inhibition may one day also find application as an anti-cancer strategy, as some UGGT substrate glycoproteins[48] are selectively up-regulated in cancer cells.[20] Replication of pathogenic enveloped viruses whose envelope glycoproteins fold under UGGT control may be impaired by UGGT inhibitors.[54] Modulation of UGGT activity would also affect adaptive immune responses triggered by antigenic peptides.[5] The strong conservation of UGGT sequence/function across eukaryotes[3] broadens the potential impact of such molecules to many fields: examples are plants as *in vivo* models to study secretion[73–75]; stress-resistant genetically modified crops[22]; or expression systems for recombinant glycoproteins.[76]

Limitations of the study

The low potency of 5M-8OH-Q in cells could be either related to low efficiency in crossing the plasma and ER membranes, or to low-specificity/off-target binding. The latter would be hardly surprising, given that the molecule was discovered as a UGGT binding fragment during an FBLD effort[34] and it has not been chemically modified to improve its potency and selectivity yet. As it is, 5M-8OH-Q is toxic *in cellula* at concentrations higher than 1 mM (Figure S5) and a dose-dependent reduction of the levels of the two UGGT substrates assayed (*Hs*ProIGF1R and *Hs*ProHexB) was observed in *ALG6*$^{-/-}$ HEK293-6E cells ("WCL" lanes in Figures 5 and 6). At present, it is unclear if these side effects are due to 5M-8OH-Q directly interacting with other cellular targets, or to indirect effects of UGGT inhibition on UGGT glycoprotein clients' folding and

levels: 5M-8OH-Q treatment, as well as inhibiting UGGT-mediated reglucosylation of *Hs*ProIGF1R and *Hs*ProHexB, may cause a decrease in their levels because both client glycoproteins fold under UGGT control.

A medicinal chemistry program that will yield the next generation of 5M-8OH-Q derivatives of improved potency and selectivity is in progress. *In silico* screening, chemical synthesis, and *in vitro* assays will be used to modify the M6-8OH-Q molecule. Chemical modifications are being introduced to the quinoline scaffold, the 5-morpholino-residue, or the 8-hydroxy group. Together with derivatives incorporating polar/non-polar residues on the remaining positions of the scaffold, these daughter molecules will generate structure-activity-relationship data toward drug-like compounds with improved UGGT inhibitory potency and selectivity.

STAR★METHODS

Detailed methods are provided in the online version of this paper and include the following:

- KEY RESOURCES TABLE
- RESOURCE AVAILABILITY
  - Lead contact
  - Materials availability
  - Data and code availability
- EXPERIMENTAL MODEL AND STUDY PARTICIPANT DETAILS
  - E. coli strains for protein production
- METHOD DETAILS
  - UGGT1 cloning, protein expression and purification
  - *Ct*UGGT$_{GT24}$ cloning, protein expression and purification
  - Crystal growth
  - X-ray data collection, processing, and model refinement
  - *In silico* modeling of the *Ct*UGGT$_{GT24}$:Man$_9$GlcNAc$_2$ complex
  - Estimation of 5M-8OH-Q: human UGGT1 K_d by STD NMR *in vitro*
  - Measurements of N-NHS-RED-*Ct*UGGT$_{GT24}$ by LEF *in vitro*
  - Purification of the 2AA-M9 and 2AA-M5-9 *N*-glycans
  - Estimation of 2AA-Man5-9:*Ct*UGGT$_{GT24}$ K_d by MST and LEF *in vitro*
  - Estimation of 5M-8OH-Q:*Ct*UGGT$_{GT24}$ K_d by LEF *in vitro*
  - Estimation of 2AA-M9:*Ct*UGGT$_{GT24}$ K_d by FPA *in vitro*
  - *In cellula* UGGT-mediated glucosylation assays
  - Viability assay for treated HEK293-6E cells
- QUANTIFICATION AND STATISTICAL ANALYSIS

SUPPLEMENTAL INFORMATION

Supplemental information can be found online at https://doi.org/10.1016/j.isci.2023.107919.

ACKNOWLEDGMENTS

We thank the members of N.Z.'s laboratory for assistance in the lab. Edward Lowe, Patrick Collins, Alice Douangamath, Jose Brandao-Neto, and the staff at beamline I04-1, at the Diamond Light Source, Harwell, England, UK, assisted with crystal growing, soaking, fishing, and X-ray data collection. Jo Nettleship at the Oxford Protein Production Facility assisted in the cloning of UGGT1. Christina Redfield assisted with the NMR measurements. The work was funded by the Glycobiology Endowment and by a University of Oxford Confidence in Concept Scheme, grant reference MRC–MC_PC_16056 (to N.Z.). P.R. was the recipient of an LISCB Wellcome Trust ISSF award, grant ref. 204801/Z/16/Z and a Wellcome Trust Seed Award in Science, grant ref. 214090/Z/18/Z. J.C.H. and A.T.C. were funded by Wellcome Trust 4-Year Studentships 106272/Z/14/Z and 097300/Z/11/Z, respectively. This work was also supported by the US Foundation for the National Institutes of Health (GM086874 to D.N.H.) and a Chemistry-Biology Interface program training grant (T32 GM139789 to K.P.G). Michela Bollati kindly gave us access to her TECAN Infinite 200 COMPlex fluorimeter. Vincenzo Pisapia pointed us to a few references describing MST experiments. R.I. was the recipient of Sardinian Regional Government Erasmus and PhD scholarships. F.B. was funded by Project IR00011– EBRAINS-Italy - - PNRR Investment thread 3.1, Action 3.1.1 - Area ESFRI H&F, financed by the European Union – NextGeneration EU (CUP B51E22000150006). N.Z. is a Fellow of Merton College, Oxford.

AUTHOR CONTRIBUTIONS

P.R., N.Z., and D.N.H. conceived and funded the study. P.R., J.C.H., S.V., and R.I. cloned, expressed, and purified UGGT1. K.H. and S.G.W. synthesized U2F. P.R., J.D.L.C., R.I., A.L., A.T.C., M.H., and S.V. expressed and purified *Ct*UGGT$_{GT24}$. P.R., J.D.L.C., R.I., M.H., A.V.C., A.T.C., and A.L.K. determined and refined the crystal structures. Y.B. contributed to structure refinement. J.L.K. carried out the NMR *in vitro* binding assays. P.R., K.P.G., D.N.H., I.Z., M.D.B., A.L., A.S., J.D.L.C., and E.B. carried out inhibitor assays. J.I.B.C., C.P.M., and Ma.Ma. carried out the *in*

silico docking. S.V. and J.B. purified the glycan samples. P.R., J.B., A.V.C., and S.V. carried out the fluorescence polarization anisotropy binding assays. P.R., F.B, Ma. Mi., and M.d.R. carried out the fluorescence and microscale thermophoresis binding assays and analyzed the binding data. All authors contributed to the writing of the manuscript.

DECLARATION OF INTERESTS

The authors declare no competing interests.

Received: November 28, 2022
Revised: July 5, 2023
Accepted: September 12, 2023
Published: September 20, 2023

REFERENCES

1. Vincenz-Donnelly, L., and Hipp, M.S. (2017). The endoplasmic reticulum: A hub of protein quality control in health and disease. Free Radic. Biol. Med. *108*, 383–393. https://doi.org/10.1016/j.freeradbiomed.2017.03.031.
2. Hebert, D.N., and Molinari, M. (2007). In and out of the ER: Protein folding, quality control, degradation, and related human diseases. Physiol. Rev. *87*, 1377–1408. https://doi.org/10.1152/physrev.00050.2006.
3. Hebert, D.N., Lamriben, L., Powers, E.T., and Kelly, J.W. (2014). The intrinsic and extrinsic effects of N-linked glycans on glycoproteostasis. Nat. Chem. Biol. *10*, 902–910.
4. Hammond, C., Braakman, I., and Helenius, A. (1994). Role of N-linked oligosaccharide recognition, glucose trimming, and calnexin in glycoprotein folding and quality control. Proc. Natl. Acad. Sci. USA *91*, 913–917.
5. Sagert, L., Winter, C., Ruppert, I., Zehetmaier, M., Thomas, C., and Tampé, R. (2023). The er folding sensor uggt1 acts on tapbpr-chaperoned peptide-free mhc i. Elife *12*, e85432. https://doi.org/10.7554/eLife.85432.
6. Caputo, A.T., Alonzi, D.S., Marti, L., Reca, I.-B., Kiappes, J.L., Struwe, W.B., Cross, A., Basu, S., Lowe, E.D., Darlot, B., et al. (2016). Structures of mammalian ER α-glucosidase II capture the binding modes of broad-spectrum iminosugar antivirals. Proc. Natl. Acad. Sci. USA *113*, E4630–E4638.
7. Warfield, K.L., Plummer, E.M., Sayce, A.C., Alonzi, D.S., Tang, W., Tyrrell, B.E., Hill, M.L., Caputo, A.T., Killingbeck, S.S., Beatty, P.R., et al. (2016). Inhibition of Endoplasmic Reticulum Glucosidases Is Required for in Vitro and in Vivo Dengue Antiviral Activity by the Iminosugar UV-4 (Antiviral research).
8. Wu, Y., Huang, X., Zheng, Z., Yang, X., Ba, Y., and Lian, J. (2021). Role and mechanism of chaperones calreticulin and ERP57 in restoring trafficking to mutant HERG-A561V protein. Int. J. Mol. Med. *48*, 159.
9. Trombetta, E.S., and Helenius, A. (1999). Glycoprotein reglucosylation and nucleotide sugar utilization in the secretory pathway: identification of a nucleoside diphosphatase in the endoplasmic reticulum. EMBO J. *18*, 3282–3292.
10. Abe, J., Takeda, Y., Kikuma, T., Kizuka, Y., Kajiura, H., Kajihara, Y., and Ito, Y. (2023). Squaryl group-modified udp analogs as inhibitors of the endoplasmic reticulum-resident folding sensor enzyme uggt. Chem. Commun. *59*, 2803–2806. https://doi.org/10.1039/D2CC06634C.
11. Totani, K., Ihara, Y., Tsujimoto, T., Matsuo, I., and Ito, Y. (2009). The recognition motif of the glycoprotein-folding sensor enzyme udp-glc:glycoprotein glucosyltransferase. Biochemistry *48*, 2933–2940. https://doi.org/10.1021/bi8020586.
12. Kudo, T., Hirano, M., Ishihara, T., Shimura, S., and Totani, K. (2014). Glycopeptide probes for understanding peptide specificity of the folding sensor enzyme uggt. Bioorg. Med. Chem. Lett. *24*, 5563–5567. https://doi.org/10.1016/j.bmcl.2014.11.013.
13. Saeed, M., Suzuki, R., Watanabe, N., Masaki, T., Tomonaga, M., Muhammad, A., Kato, T., Matsuura, Y., Watanabe, H., Wakita, T., and Suzuki, T. (2011). Role of the endoplasmic reticulum-associated degradation (ERAD) pathway in degradation of hepatitis c virus envelope proteins and production of virus particles. J. Biol. Chem. *286*, 37264–37273. https://doi.org/10.1074/jbc.m111.259085.
14. Huang, J., Yin, H., Yin, P., Jian, X., Song, S., Luan, J., and Zhang, L. (2019). SR-BI Interactome Analysis Reveals a Proviral Role for UGGT1 in Hepatitis C Virus Entry. Front. Microbiol. *10*, 2043.
15. Ruan, J., Rothan, H.A., Zhong, Y., Yan, W., Henderson, M.J., Chen, F., and Fang, S. (2019). A small molecule inhibitor of ER-to-cytosol protein dislocation exhibits anti-dengue and anti-zika virus activity. Sci. Rep. *9*, 10901. https://doi.org/10.1038/s41598-019-47532-7.
16. Amara, J.F., Cheng, S.H., and Smith, A.E. (1992). Intracellular protein trafficking defects in human disease. Trends Cell Biol. *2*, 145–149. https://doi.org/10.1016/0962-8924(92)90101-r.
17. Parodi, A.J., Caramelo, J.J., and D'Alessio, C. (2014). UDP-Glucose: Glycoprotein Glucosyltransferase 1,2 (UGGT1,2). In Handbook of Glycosyltransferases and Related Genes (Springer Japan), pp. 15–30.
18. Kuribara, T., Imagawa, A., Hirano, M., Ito, Y., and Totani, K. (2020). Metabolic syndrome perturbs deglucosylation and reglucosylation in the glycoprotein folding cycle. FEBS Lett. *594*, 1759–1769. https://doi.org/10.1002/1873-3468.13780.
19. Liu, Y., and Ye, Y. (2011). Proteostasis regulation at the endoplasmic reticulum: a new perturbation site for targeted cancer therapy. Cell Res. *21*, 867–883.
20. Tax, G., Lia, A., Santino, A., and Roversi, P. (2019). Modulation of ERQC and ERAD: A Broad-Spectrum Spanner in the Works of Cancer Cells? JAMA Oncol. *2019*, 8384913.
21. McMahon, M., Samali, A., and Chevet, E. (2021). Maintenance of Endoplasmic Reticulum Protein Homeostasis in Cancer: Friend or Foe (Springer International Publishing), pp. 197–214. ISBN 978-3-030-67696-42021. https://doi.org/10.1007/978-3-030-67696-4_10.
22. Liu, J.-X., Srivastava, R., Che, P., and Howell, S.H. (2007). Salt stress responses in arabidopsis utilize a signal transduction pathway related to endoplasmic reticulum stress signaling. Plant J. *51*, 897–909. https://doi.org/10.1111/j.1365-313x.2007.03195.x.
23. Valente, M.A.S., Faria, J.A.Q.A., Soares-Ramos, J.R.L., Reis, P.A.B., Pinheiro, G.L., Piovesan, N.D., Morais, A.T., Menezes, C.C., Cano, M.A.O., Fietto, L.G., et al. (2009). The ER luminal binding protein (BiP) mediates an increase in drought tolerance in soybean and delays drought-induced leaf senescence in soybean and tobacco. J. Exp. Bot. *60*, 533–546. https://doi.org/10.1093/jxb/ern296.
24. Jia, X.-Y., Xu, C.-Y., Jing, R.-L., Li, R.-Z., Mao, X.-G., Wang, J.-P., and Chang, X.-P. (2008). Molecular cloning and characterization of wheat calreticulin (CRT) gene involved in drought-stressed responses. J. Exp. Bot. *59*, 739–751. https://doi.org/10.1093/jxb/erm369.
25. Sekiya, M., Maruko-Otake, A., Hearn, S., Sakakibara, Y., Fujisaki, N., Suzuki, E., Ando, K., and Iijima, K.M. (2017). EDEM function in ERAD protects against chronic ER proteinopathy and age-related physiological decline in drosophila. Dev. Cell *41*, 652–664.e5. https://doi.org/10.1016/j.devcel.2017.05.019.
26. Ciulli, A., Williams, G., Smith, A.G., Blundell, T.L., and Abell, C. (2006). Probing hot spots at protein-ligand binding sites: a fragment-based approach using biophysical methods. J. Med. Chem. *49*, 4992–5000.
27. Murray, C.W., and Blundell, T.L. (2010). Structural biology in fragment-based drug design. Curr. Opin. Struct. Biol. *20*, 497–507.
28. Chen, X., Qin, S., Chen, S., Li, J., Li, L., Wang, Z., Wang, Q., Lin, J., Yang, C., and Shui, W. (2015). A ligand-observed mass spectrometry approach integrated into the fragment based lead discovery pipeline. Sci. Rep. *5*, 8361.
29. Radoux, C.J., Olsson, T.S.G., Pitt, W.R., Groom, C.R., and Blundell, T.L. (2016). Identifying Interactions that Determine Fragment Binding at Protein Hotspots. J. Med. Chem. *59*, 4314–4325.
30. Roversi, P., Marti, L., Caputo, A.T., Alonzi, D.S., Hill, J.C., Dent, K.C., Kumar, A., Levasseur, M.D., Lia, A., Waksman, T., et al. (2017a). Interdomain conformational flexibility underpins the activity of uggt, the eukaryotic glycoprotein secretion checkpoint. Proc. Natl. Acad. Sci. USA *114*,

8544–8549. https://doi.org/10.1073/pnas.1703682114.
31. Satoh, T., Song, C., Zhu, T., Toshimori, T., Murata, K., Hayashi, Y., Kamikubo, H., Uchihashi, T., and Kato, K. (2017). Visualisation of a flexible modular structure of the ER folding-sensor enzyme UGGT. Sci. Rep. *7*, 12142.
32. Modenutti, C.P., Blanco Capurro, J.I., Ibba, R., Alonzi, D.S., Song, M.N., Vasiljević, S., Kumar, A., Chandran, A.V., Tax, G., Marti, L., et al. (2021). Clamping, bending, and twisting inter-domain motions in the misfold-recognizing portion of udp-glucose: Glycoprotein glucosyltransferase. Structure *29*, 357–370.e9. https://doi.org/10.1016/j.str.2020.11.017.
33. Aricescu, A.R., Lu, W., and Jones, E.Y. (2006). A time- and cost-efficient system for high-level protein production in mammalian cells. Acta Crystallogr. D Biol. Crystallogr. *62*, 1243–1250.
34. Caputo, A.T., Ibba, R., Le Cornu, J.D., Darlot, B., Hensen, M., Lipp, C.B., Marcianò, G., Vasiljević, S., Zitzmann, N., and Roversi, P. (2022). Crystal polymorphism in fragment-based lead discovery of ligands of the catalytic domain of UGGT, the glycoprotein folding quality control checkpoint. Front. Mol. Biosci. *9*, 960248. https://doi.org/10.3389/fmolb.2022.960248.
35. Tessier, D.C., Dignard, D., Zapun, A., Radominska-Pandya, A., Parodi, A.J., Bergeron, J.J., and Thomas, D.Y. (2000). Cloning and characterization of mammalian UDP-glucose glycoprotein: glucosyltransferase and the development of a specific substrate for this enzyme. Glycobiology *10*, 403–412.
36. Sprong, H., Degroote, S., Nilsson, T., Kawakita, M., Ishida, N., van der Sluijs, P., and van Meer, G. (2003). Association of the Golgi UDP-galactose transporter with UDP-galactose:ceramide galactosyltransferase allows UDP-galactose import in the endoplasmic reticulum. Mol. Biol. Cell *14*, 3482–3493.
37. Maszczak-Seneczko, D., Olczak, T., and Olczak, M. (2011). Subcellular localization of UDP-GlcNAc, UDP-Gal and SLC35B4 transporters. Acta Biochim. Pol. *58*, 413–419.
38. Nakajima, K., Kizuka, Y., Yamaguchi, Y., Hirabayashi, Y., Takahashi, K., Yuzawa, Y., and Taniguchi, N. (2018). Identification and characterization of UDP-mannose in human cell lines and mouse organs: Differential distribution across brain regions and organs. Biochem. Biophys. Res. Commun. *495*, 401–407.
39. Miyagawa, A., Totani, K., Matsuo, I., and Ito, Y. (2010). Promiscuous activity of er glucosidase ii discovered through donor specificity analysis of uggt. Biochem. Biophys. Res. Commun. *403*, 322–328. https://doi.org/10.1016/j.bbrc.2010.11.027.
40. McNicholas, S., and Agirre, J. (2017). Glycoblocks: a schematic three-dimensional representation for glycans and their interactions. Acta Crystallogr. D Struct. Biol. *73*, 187–194.
41. Lanzarotti, E., Defelipe, L.A., Marti, M.A., and Turjanski, A.G. (2020). Aromatic clusters in protein-protein and protein-drug complexes. J. Cheminf. *12*, 30.
42. Roversi, P., Marti, L., Caputo, A.T., Alonzi, D.S., Hill, J.C., Dent, K.C., Kumar, A., Levasseur, M.D., Lia, A., Waksman, T., et al. (2017b). Interdomain conformational flexibility underpins the activity of uggt, the eukaryotic glycoprotein secretion checkpoint. Proc. Natl. Acad. Sci. USA *114*, 8544–8549. https://doi.org/10.1073/pnas.1703682114.
43. Sousa, M.C., Ferrero-Garcia, M.A., and Parodi, A.J. (1992). Recognition of the oligosaccharide and protein moieties of glycoproteins by the UDP-Glc:glycoprotein glucosyltransferase. Biochemistry *31*, 97–105.
44. Sousa, M.C., and Parodi, A.J. (1996). The interaction of the UDP-GLC:glycoprotein glucosyltransferase with the acceptor glycoprotein. Cell. Mol. Biol. *42*, 609–616.
45. Lee, E., Shim, S.-H., and Cho, M. (2018). Fluorescence enhancement of a ligand-activated fluorescent protein induced by collective noncovalent interactions. Chem. Sci. *9*, 8325–8336. https://doi.org/10.1039/C8SC03558J.
46. Bartoschik, T., Zoephel, A., Rumpel, K., Ciulli, A., and Heffern, C. MSTMicroScale thermophoresis (MST)and TRICTemperature related intensity change (TRIC) Technology to Reliably Study PROTACProteolysis-targeting chimeras (PROTACs) Binary and Ternary Binding in Drug Development (115–133). New York, NY: Springer US. ISBN 978-1-0716-1665-9 (2021):(115–133). URL: https://doi.org/10.1007/978-1-0716-1665-9_6. doi:10.1007/978-1-0716-1665-9_6
47. Pearse, B.R., Gabriel, L., Wang, N., and Hebert, D.N. (2008). A cell-based reglucosylation assay demonstrates the role of GT1 in the quality control of a maturing glycoprotein. J. Cell Biol. *181*, 309–320.
48. Adams, B.M., Canniff, N.P., Guay, K.P., Larsen, I.S.B., and Hebert, D.N. (2020). Quantitative Glycoproteomics Reveals Substrate Selectivity of the ER Protein Quality Control Sensors UGGT1 and UGGT2, *9* (eLife).
49. Aebi, M. (2013). N-linked protein glycosylation in the ER. Biochim. Biophys. Acta *1833*, 2430–2437.
50. Adams, B.M., Canniff, N.P., Guay, K.P., and Hebert, D.N. (2021). The Role of Endoplasmic Reticulum Chaperones in Protein Folding and Quality Control. Prog. Mol. Subcell. Biol. *59*, 27–50.
51. Arnold, S.M., Fessler, L.I., Fessler, J.H., and Kaufman, R.J. (2000). Two homologues encoding human UDP-glucose:glycoprotein glucosyltransferase differ in mRNA expression and enzymatic activity. Biochemistry *39*, 2149–2163.
52. Blanco-Herrera, F., Moreno, A.A., Tapia, R., Reyes, F., Araya, M., D'Alessio, C., Parodi, A., and Orellana, A. (2015). The UDP-glucose: glycoprotein glucosyltransferase (UGGT), a key enzyme in ER quality control, plays a significant role in plant growth as well as biotic and abiotic stress in Arabidopsis thaliana. BMC Plant Biol. *15*, 127.
53. Trombetta, S.E., Bosch, M., and Parodi, A.J. (1989). Glucosylation of glycoproteins by mammalian, plant, fungal, and trypanosomatid protozoa microsomal membranes. Biochemistry *28*, 8108–8116. https://doi.org/10.1021/bi00446a022.
54. Dalziel, M., Crispin, M., Scanlan, C.N., Zitzmann, N., and Dwek, R.A. (2014). Emerging principles for the therapeutic exploitation of glycosylation. Science *343*, 1235681.
55. Trombetta, E.S., and Helenius, A. (1999). Glycoprotein reglucosylation and nucleotide sugar utilization in the secretory pathway: identification of a nucleoside diphosphatase in the endoplasmic reticulum. EMBO J. *18*, 3282–3292. https://doi.org/10.1093/emboj/18.12.3282.
56. Mishra, A., Periasamy, N., Patankar, M.P., and Narasimhan, K. (2005). Synthesis and characterisation of soluble aluminium complex dyes based on 5-substituted-8-hydroxyquinoline derivatives for oled applications. Dyes Pigments *66*, 89–97. https://doi.org/10.1016/j.dyepig.2004.09.004.
57. Wang, F., Peng, R., and Sha, Y. (2008). Selective dendritic fluorescent sensors for Zn(II). Molecules *13*, 922–930.
58. Kumar, S., Shah, P., Tripathi, S.K., Khan, S.I., and Singh, I.P. (2022). Synthesis and In Vitro Evaluation of Hydrazonomethyl-Quinolin-8-ol and Pyrazol-3-yl-Quinolin-8-ol Derivatives for Antimicrobial and Antimalarial Potential. Med. Chem. *18*, 949–969. https://doi.org/10.2174/1573406418666220303144929. http://www.eurekaselect.com/article/121293.
59. Al Busafi, S.N., Suliman, F., and Al-Alawi, Z.R. (2014). 8-hydroxyquinoline and its Derivatives: Synthesis and Applications. https://www.rroij.com/open-access/8hydroxyquinoline-and-its-derivatives-synthesis-and-applications-.php?aid=33914.
60. Yañez, O., Osorio, M.I., Uriarte, E., Areche, C., Tiznado, W., Pérez-Donoso, J.M., García-Beltrán, O., and González-Nilo, F. (2020). In Silico Study of Coumarins and Quinolines Derivatives as Potent Inhibitors of SARS-CoV-2 Main Protease. Front. Chem. *8*, 595097.
61. Albesa-Jové, D., Cifuente, J.O., Trastoy, B., and Guerin, M.E. (2019). Chapter fifteen - quick-soaking of crystals reveals unprecedented insights into the catalytic mechanism of glycosyltransferases. In Chemical and Synthetic Biology Approaches To Understand Cellular Functions - Part A vol. 621 of Methods in Enzymology, A.K. Shukla, ed. (Academic Press), pp. 261–279. https://doi.org/10.1016/bs.mie.2019.02.034.
62. Shoji, E., Miyatake, K., Hlil, A.R., Hay, A.S., Maindron, T., Jousseaume, V., Dodelet, J.P., Tao, Y., and D'iorio, M. (2003). Immiscible polymers in double spin-coated electroluminescent devices containing phenyl-substituted tris(8-hydroxyquinoline) aluminum derivatives soluble in a host polymer. J. Polym. Sci. A. Polym. Chem. *41*, 3006–3016.
63. King, O.N.F., Li, X.S., Sakurai, M., Kawamura, A., Rose, N.R., Ng, S.S., Quinn, A.M., Rai, G., Mott, B.T., Beswick, P., et al. (2010). Quantitative high-throughput screening identifies 8-hydroxyquinolines as cell-active histone demethylase inhibitors. PLoS One *5*, e15535. https://doi.org/10.1371/journal.pone.0015535.
64. Hopkinson, R.J., Tumber, A., Yapp, C., Chowdhury, R., Aik, W., Che, K.H., Li, X.S., Kristensen, J.B.L., King, O.N.F., Chan, M.C., et al. (2013). 5-carboxy-8-hydroxyquinoline is a broad spectrum 2-oxoglutarate oxygenase inhibitor which causes iron translocation. Chem. Sci. *4*, 3110–3117. https://doi.org/10.1039/C3SC51122G.
65. Aik, W., Demetriades, M., Hamdan, M.K.K., Bagg, E.A.L., Yeoh, K.K., Lejeune, C., Zhang, Z., McDonough, M.A., and Schofield, C.J. (2013). Structural basis for inhibition of the fat mass and obesity associated protein (fto). J. Med. Chem. *56*, 3680–3688. https://doi.org/10.1021/jm400193d.
66. Moon, H., Han, S., Park, H., and Choe, J. (2010). Crystal structures of human fih-1 in complex with quinol family inhibitors. Mol. Cell. *29*, 471–474.

67. Esposito, C., Wiedmer, L., and Caflisch, A. (2018). In silico identification of jmjd3 demethylase inhibitors. J. Chem. Inf. Model. *58*, 2151–2163. https://doi.org/10.1021/acs.jcim.8b00539.
68. Xing, J., Zhang, R., Jiang, X., Hu, T., Wang, X., Qiao, G., Wang, J., Yang, F., Luo, X., Chen, K., et al. (2019). Rational design of 5-((1h-imidazol-1-yl)methyl)quinolin-8-ol derivatives as novel bromodomain-containing protein 4 inhibitors. Eur. J. Med. Chem. *163*, 281–294. https://doi.org/10.1016/j.ejmech.2018.11.018.
69. Chen, W., Zhang, H., Chen, Z., Jiang, H., Liao, L., Fan, S., Xing, J., Xie, Y., Chen, S., Ding, H., et al. (2018). Development and evaluation of a novel series of nitroxoline-derived bet inhibitors with antitumor activity in renal cell carcinoma. Oncogenesis *7*, 83. https://doi.org/10.1038/s41389-018-0093-z.
70. Qin, J., Xie, P., Ventocilla, C., Zhou, G., Vultur, A., Chen, Q., Liu, Q., Herlyn, M., Winkler, J., and Marmorstein, R. (2012). Identification of a novel family of brafv600e inhibitors. J. Med. Chem. *55*, 5220–5230. https://doi.org/10.1021/jm3004416.
71. Buchler, I., Akuma, D., Au, V., Carr, G., de León, P., DePasquale, M., Ernst, G., Huang, Y., Kimos, M., Kolobova, A., et al. (2018). Optimization of 8-hydroxyquinolines as inhibitors of catechol o-methyltransferase. J. Med. Chem. *61*, 9647–9665. https://doi.org/10.1021/acs.jmedchem.8b01126.
72. McLean, L.R., Zhang, Y., Li, H., Li, Z., Lukasczyk, U., Choi, Y.-M., Han, Z., Prisco, J., Fordham, J., Tsay, J.T., et al. (2009). Discovery of covalent inhibitors for mif tautomerase via cocrystal structures with phantom hits from virtual screening. Bioorg. Med. Chem. Lett. *19*, 6717–6720. https://doi.org/10.1016/j.bmcl.2009.09.106.
73. Vergara, D., de Domenico, S., Maffia, M., Piro, G., and Di Sansebastiano, G.P. (2015). Transgenic plants as low-cost platform for chemotherapeutic drugs screening. Int. J. Mol. Sci. *16*, 2174–2186. https://doi.org/10.3390/ijms16012174.
74. Marti, L., Lia, A., Reca, I.-B., Roversi, P., Santino, A., and Zitzmann, N. (2018). In planta preliminary screening of er glycoprotein folding quality control (erqc) modulators. Int. J. Mol. Sci. *19*, 2135. https://www.mdpi.com/1422-0067/19/7/2135.
75. Lia, A., Gallo, A., Marti, L., Roversi, P., and Santino, A. (2018). Efr-mediated innate immune response in arabidopsis thaliana is a useful tool for identification of novel erqc modulators. Genes *10*, 15. https://doi.org/10.3390/genes10010015.
76. Ko, K., Ahn, M.-H., Song, M., Choo, Y.-K., Kim, H.S., Ko, K., and Joung, H. (2008). Glyco-engineering of biotherapeutic proteins in plants. Mol. Cell. *25*, 494–503.
77. Vonrhein, C., Flensburg, C., Keller, P., Sharff, A., Smart, O., Paciorek, W., Womack, T., and Bricogne, G. (2011). Data processing and analysis with the autoPROC toolbox. Acta Crystallogr. D Biol. Crystallogr. *67*, 293–302.
78. Emsley, P., Lohkamp, B., Scott, W.G., and Cowtan, K. (2010). Features and development of Coot. Acta crystallographica. Acta Crystallogr. D Biol. Crystallogr. *66*, 486–501.
79. Blanc, E., Roversi, P., Vonrhein, C., Flensburg, C., Lea, S.M., and Bricogne, G. (2004). Refinement of severely incomplete structures with maximum likelihood in BUSTER-TNT. Acta Crystallogr. D Biol. Crystallogr. *60*, 2210–2221.
80. Singh, A., Montgomery, D., Xue, X., Foley, B.L., and Woods, R.J. (2019). GAG Builder: a web-tool for modeling 3D structures of glycosaminoglycans. Glycobiology *29*, 515–518.
81. Arcon, J.P., Modenutti, C.P., Avendaño, D., Lopez, E.D., Defelipe, L.A., Ambrosio, F.A., Turjanski, A.G., Forli, S., and Marti, M.A. (2019). AutoDock Bias: improving binding mode prediction and virtual screening using known protein–ligand interactions. Bioinformatics *35*, 3836–3838. https://doi.org/10.1093/bioinformatics/btz152.
82. Morris, G.M., Huey, R., Lindstrom, W., Sanner, M.F., Belew, R.K., Goodsell, D.S., and Olson, A.J. (2009). Autodock4 and autodocktools4: Automated docking with selective receptor flexibility. J. Comput. Chem. *30*, 2785–2791. https://doi.org/10.1002/jcc.21256.
83. Gorrec, F. (2009). The MORPHEUS protein crystallization screen. J. Appl. Crystallogr. *42*, 1035–1042.
84. Gorrec, F. (2015). The MORPHEUS II protein crystallization screen. Acta Crystallogr. F Struct. Biol. Commun. *71*, 831–837.
85. Morgan, J.L.W., McNamara, J.T., Fischer, M., Rich, J., Chen, H.-M., Withers, S.G., and Zimmer, J. (2016). Observing cellulose biosynthesis and membrane translocation in crystallo. Nature *531*, 329–334.
86. Bricogne, G., Blanc, E., Brandl, M., Flensburg, C., Keller, P., Paciorek, W., Roversi, P., Sharff, A., Smart, O.S., Vonrhein, C., and TO, W. (2017). BUSTER 2.10.3. In BUSTER 2.10.3.
87. Emsley, P., and Cowtan, K. (2004). Coot: model-building tools for molecular graphics. Acta Crystallogr. D Biol. Crystallogr. *60*, 2126–2132.
88. Modenutti, C., Gauto, D., Radusky, L., Blanco, J., Turjanski, A., Hajos, S., and Marti, M. (2015). Using crystallographic water properties for the analysis and prediction of lectin–carbohydrate complex structures. Glycobiology *25*, 181–196. https://doi.org/10.1093/glycob/cwu102.
89. Nivedha, A.K., Makeneni, S., Foley, B.L., Tessier, M.B., and Woods, R.J. (2014). Importance of ligand conformational energies in carbohydrate docking: Sorting the wheat from the chaff. J. Comput. Chem. *35*, 526–539. https://doi.org/10.1002/jcc.23517.
90. Woods, R.J. (2018). Predicting the structures of glycans, glycoproteins, and their complexes. Chem. Rev. *118*, 8005–8024. https://doi.org/10.1021/acs.chemrev.8b00032.
91. Kirschner, K.N., Yongye, A.B., Tschampel, S.M., González-Outeiriño, J., Daniels, C.R., Foley, B.L., and Woods, R.J. (2008). Glycam06: A generalizable biomolecular force field. carbohydrates. J. Comput. Chem. *29*, 622–655. https://doi.org/10.1002/jcc.20820.
92. Blanco Capurro, J.I., Di Paola, M., Gamarra, M.D., Martí, M.A., and Modenutti, C.P. (2019). An efficient use of X-ray information, homology modeling, molecular dynamics and knowledge-based docking techniques to predict protein–monosaccharide complexes. Glycobiology *29*, 124–136.
93. Makeneni, S., Thieker, D.F., and Woods, R.J. (2018). Applying pose clustering and md simulations to eliminate false positives in molecular docking. J. Chem. Inf. Model. *58*, 605–614. https://doi.org/10.1021/acs.jcim.7b00588.
94. Dunlop, D.C., Bonomelli, C., Mansab, F., Vasiljević, S., Doores, K.J., Wormald, M.R., Palma, A.S., Feizi, T., Harvey, D.J., Dwek, R.A., et al. (2010). Polysaccharide mimicry of the epitope of the broadly neutralizing anti-HIV antibody, 2G12, induces enhanced antibody responses to self oligomannose glycans. Glycobiology *20*, 812–823.

STAR★METHODS

KEY RESOURCES TABLE

REAGENT or RESOURCE	SOURCE	IDENTIFIER
Antibodies		
Anti-IGF1R	Cell Signaling	Cat#9750;RRID:AB_10950969
Anti-HexB	Abcam	Cat#ab140649;RRID:AB_3065101
Anti-GAPDH	Millipore Sigma	Cat#MAB374;RRID:AB_2107445
Bacterial and virus strains		
E.coli DH5-α	New England Bioscience	Cat# C2987I
Chemicals, peptides, and recombinant proteins		
AgeI-HF	New England Biolabs	Cat# R3552S
KpnI-HF	New England Biolabs	Cat# R3142S
CutSmart Buffer	New England Biolabs	Cat# B7204 actually replaced by Cat# B6004S
QIAquick gel extraction kit	QIAGEN	Cat# 28706
In-Fusion Cloning	TakaraBio Ltd	Cat# 638947
Kifunensine	Cayman Chemical	Cat# 109944-15-2
Anthranilic Acid	Sigma-Aldrich	Cat# A89855
MORPHEUS Crystallisation Screen	Molecular Dimensions	Cat# MD1–47
HEPES	Sigma-Aldrich	Cat# H3375
Imidazole	Honeywell Fluka	Cat# 56750
Deposited data		
Python code	This paper	https://doi.org/10.5281/zenodo.8305097
$CtUGGT_{GT24}$	This paper	PDB ID 7ZKC
$^{U2F}CtUGGT_{GT24}$	This paper	PDB ID 7ZLU
$^{5M-8OH-Q}CtUGGT_{GT24}$	This paper	PDB ID 7ZLL
Experimental models: Cell lines		
HEK FreeStyleTM 293F cells	ThermoFisher Scientific	Cat# R79007
HEK293-EBNA1-6E ALG6$^{-/-}$	Adams et al.[48]	
HEK293-EBNA1-6E ALG6/UGGT1$^{-/-}$	Adams et al.[48]	
HEK293-EBNA1-6E ALG6/UGGT2$^{-/-}$	Adams et al.[48]	
HEK293-EBNA1-6E ALG6/UGGT1/2$^{-/-}$	Adams et al.[48]	
Oligonucleotides		
OPPF UGGT1 Fwd gcgtagctgaaaccggc GACTCAAAAGCCATTACAACCTCTCT	Eurofins Scientific	NA
OPPF UGGT1 Rev gtgatggtgatgttt TTTCTGAGGACCTTCTCGGCTTGG	Eurofins Scientific	NA
Recombinant DNA		
UGGT1-pUC57	Genscript	NA
pOPINTTGneo:hUGGT1 plasmid	This paper	NA
Software and algorithms		
autoPROC	Vonrhein et al.[77]	Version 1.0.5
Coot	Emsley et al.[78]	Version 0.9
BUSTER	Blanc et al.[79]	Version 2.10.3

(*Continued on next page*)

Continued

REAGENT or RESOURCE	SOURCE	IDENTIFIER
GLYCAM-web	Singh et al.,[80]	Version 1.0
AutoDock-Bias	Arcon et al.,[81]	Version 1.0
AutoDock4	Morris et al.,[82]	Version 4.0

RESOURCE AVAILABILITY

Lead contact

Further information and requests for resources and reagents should be directed to and will be fulfilled by the Lead Contact, Pietro Roversi (pietro.roversi@cnr.it).

Materials availability

The pOPINTTGneo:hUGGT1 plasmid generated in this study is available for distribution. This study did not generate any other unique reagents. Further information and requests for resources and reagents should be directed to and will be fulfilled by the lead contact, Pietro Roversi (pietro.roversi@cnr.it).

Data and code availability

- Crystal structure coordinates and structure factor files (mmCIF format) were deposited and are publicly accessible in the protein databank (PDB) as PDB IDs 7ZKC (*Ct*UGGT$_{GT24}$), 7ZLU (^{U2F}*Ct*UGGT$_{GT24}$) and 7ZLL ($^{5M\text{-}8OH\text{-}Q}$*Ct*UGGT$_{GT24}$). Accession numbers are also listed in the key resources table.
- All original code has been deposited at Zenodo (https://doi.org/10.5281/zenodo.8305097) and is publicly available as of the date of publication. The DOI is listed in the key resources table.
- Any additional information required to reanalyze the data reported in this paper is available from the lead contact upon request.

EXPERIMENTAL MODEL AND STUDY PARTICIPANT DETAILS

E. coli strains for protein production

DH5α chemically competent *E. coli* was used to make the pHLsec:*Ct*UGGT, pHLsec:*Ct*UGGT$_{GT24}$ and pOPINTTGneo:hUGGT1 plasmids.

METHOD DETAILS

UGGT1 cloning, protein expression and purification

The C-terminally His-tagged construct encoding human UGGT1 residues 43-1551 was PCR-amplified from the commercially sourced vector UGGT1-pUC57 (GenScript) with primers: OPPF_UGGT1_Fwd: gcgtagctgaaaccggcGACTCAAAAGCCATTACAACCTCTCT OPPF_UGGT1_Rev: gtgatggtgatgtttTTTCTGAGGACCTTCTCGGCTTGG. These primers were designed to surround the insert with an N-terminal AgeI restriction site and a C-terminal KpnI site (after the C-terminal 6xHis tag and the stop codon). The amplified DNA was run on a 0.8% agarose gel and the correctly-sized fragment excised and purified using the QIAquick Gel Extraction Kit (QIAgen). The pOPINTTGneo plasmid was linearised with 20 units of both AgeI-HF and KpnI-HF restriction enzymes, incubated with 1x CutSmart Buffer (New England BioLabs) and 500ng of pHLSec DNA and digested at 37°C overnight. Both the linearised pOPINTTGneo and the UGGT1 insert DNA were run on a 0.8% agarose gel and the correctly-sized fragments excised and purified using the QIAquick Gel Extraction Kit (QIAgen). DNA ligation of the linearised pOPINTTGneo vector and the human UGGT1 insert was achieved by In-fusion™ligation-independent cloning (Takara Ltd.)

Transfection of HEK293F cells with the pOPINTTGneo-hUGGT1 plasmid and expression of the recombinant human UGGT1 protein were carried out a protocol equivalent to the one described for expression of *Ct*UGGT,[42] using the FreeStyle 293 Expression System (Thermo Fisher Scientific) and following the manufacturer's protocol.

Immobilised Metal Affinity Chromatography (IMAC): after 5 days, the cells' supernatant was applied onto a Ni-affinity column equilibrated with PBS binding buffer. The protein was eluted with a 20 Column Volumes linear gradient elution at a flow rate of 1 ml/min increasing from 0% to 100% elution buffer (PBS plus 500 mM Imidazole).

Size Exclusion Chromatography (SEC): the IMAC step eluate was pooled and concentrated to 0.5 mL using a 100kDa spin concentrator. The sample was then loaded on a 0.5 mL loop and applied to a 10/300 Sephadex 200 column running at 1 mL/min. The SEC buffer was 20 mM MES pH 6.5, 50 mM NaCl, 1 mM $CaCl_2$, 1 mM UDP. The latter buffer was arrived at by Differential Scanning Fluorimetry (DSF): the stability of UGGT1 is greatly increased through the addition of $CaCl_2$, with an increase in melting temperature Tm of 3.0°C and addition of UDP, with an increase in Tm of 1.1 °C. The DSF experiment also showed a clear preference for lower salt concentrations and a slightly more acidic pH.

*Ct*UGGT$_{GT24}$ cloning, protein expression and purification

*Ct*UGGT$_{GT24}$ was cloned, expressed and purified as described in.[34]

Crystal growth

Crystals were grown at 18°C in sitting drops by the vapour diffusion method, set up with a Mosquito liquid handling robot (TTP Labtech). Crystallisation drops had an initial volume of 200 nL. The volume ratio of protein to precipitant was either 1:1 or 2:1.

*Ct*UGGT$_{GT24}$ crystallisation

A crystal of *Ct*UGGT$_{GT24}$ grew in one week in a 1:1 mixture of *Ct*UGGT$_{GT24}$ at 6 mg/mL and Morpheus screen condition 1-1 composed of 0.06 M Divalents, 0.1 M Buffer System 1 pH 6.5, 30% v/v Precipitant Mix 1.[83,84]

*Ct*UGGT$_{GT24}$:U2F co-crystallisation

U2F was synthesised as described in.[85] A crystal of *Ct*UGGT$_{GT24}$:U2F grew in one week in a 1:1 mixture of *Ct*UGGT$_{GT24}$ at 12 mg/mL, 2 mM $CaCl_2$, 1.25 mM U2F and Morpheus screen condition 2-17 composed of 0.12 M Monosaccharides, 0.1 M Buffer System 2 pH 7.5, 30% v/v Precipitant Mix 1.[83,84]

FBLD of UGGT ligands

Details of the study are available in.[34]

$^{5M\text{-}8OH\text{-}Q}$*Ct*UGGT$_{GT24}$ co-crystallisation

A crystal of $^{5M\text{-}8OH\text{-}Q}$*Ct*UGGT$_{GT24}$ grew in one week in a 1:1 mixture of *Ct*UGGT$_{GT24}$ at 6.5 mg/mL, 10 mM 5M-8OH-Q in DMSO and Morpheus screen condition 1-1 composed of 0.06M Divalents, 0.1 M Buffer System 1 pH 6.5, 30% v/v Precipitant Mix 1.[83,84]

X-ray data collection, processing, and model refinement

X-ray data collection beamlines and data collection parameters are listed in Table S1. Data processing was carried out in autoPROC.[77] The model refinement and ligand fitting were carried out with BUSTER[79,86] and Coot.[78,87] Refinement statistics are listed in Table S2.

In silico modeling of the *Ct*UGGT$_{GT24}$:Man$_9$GlcNAc$_2$ complex

Due to the limitations of conventional docking methods in dealing with oligosaccharides larger than five units,[88] we used a hierarchical approach that combined biased docking and Molecular Dynamics (MD) in order to build a model of the Man$_9$GlcNAc$_2$ glycan (M9) bound to *Ct*UGGT$_{GT24}$.

As a rule, carbohydrate ligands bind to proteins in a conformation close to one of the gas-phase energy minima. The latter mainly depend on the values of the dihedral angles of each glycosidic bond.[89] Although each of these can only assume a few possible conformations, the M9 glycan has 70 torsional degrees of freedom overall (including OH and CH_3 groups, glycosidic linkages, etc.). This number is such that docking algorithms cannot handle full torsional optimisation.[90]

We therefore generated nine initial Man$_9$GlcNAc$_2$ conformations using the GLYCAM-web server at https://glycam.org/lib/load/hmlib/.[80] Each of these structures was then optimized using MD in explicit solvent,[91] thus broadening the M9 conformational space spanned by the structures.

The results were clustered using only the poses of furanose rings with a 1.4 A of tolerance[92] and 250 representative Man$_9$GlcNAc$_2$ conformations were selected and underwent the analysis described here below:

1. we first aligned the acceptor Man residue of the Man$_9$GlcNAc$_2$ N-linked glycan (i.e. the terminal Man residue of its A-branch, Man "G" (Figure 2B) such that its C1 atom pointed towards the O3 atom of the UDP-Glc molecule in our ^{U2F}*Ct*UGGT$_{GT24}$ structure (see also the structure of *Td*UGGT$_{GT24}$ in complex with UDP-Glc, PDB ID 5H18,[31]). This assumes that this Man "G" residue docks in the active site such that upon Glc transfer, a β(1-3) linkage will form;
2. then, using that Man "G" residue orientation as a constraint, we performed multiple docking simulations of the Man$_9$GlcNAc$_2$ ligand, using the AutoDock-Bias protocol ([81], modified as described in[88]), and keeping all torsional degrees of freedom fixed;
3. the results were clustered and the three best ranking poses selected for further refinement using MD simulations. Starting from each complex, Molecular Dynamics was used to relax the Man$_9$GlcNAc$_2$ structure onto the *Ct*UGGT$_{GT24}$ domain, using the protocol described in[93];
4. since the final pose for each of the three best MD refinements was almost identical (RMSD < 2 Å), we performed a final single-point energy calculation with AutoDock4[82] to select the best complex.

Estimation of 5M-8OH-Q: human UGGT1 K_d by STD NMR *in vitro*

For each 5M-8OH-Q concentration, a 1 μM solution of human UGGT1 was incubated with 5M-8OH-Q in PBS prepared in D_2O. Briefly, 100 μL of a human UGGT1 stock solution at 2 μM and 100 μL of the dilution series of molecule at twice the desired final concentration were mixed and

left to equilibrate for at least one hour. High and low concentrations were measured alternately to remove any time effects. As a further control the first sample was remeasured after the last one to confirm that the STD had not changed. The signal/noise was not high enough at 5M-8OH-Q concentrations below 100 μM. No STD was observed with the maximum tested dose (2 mM 5M-8OH-Q) in absence of human UGGT1.

Measurements of N-NHS-RED-*Ct*UGGT$_{GT24}$ by LEF *in vitro*

Fluorescence spectra were measured in a quartz cuvette on a Cary Eclipse fluorescence spectrophotometer. λ_{excit}=600 nm, λ_{emiss}=620-700(5) nm. 5M-8OH-Q fluorescence: 1 μL of 5M-8OH-Q 250 mM in DMSO was added to 99 μL of a buffer 100 mM NaCl and 20 mM HEPES pH 7.4. *Ct*UGGT$_{GT24}$ fluorescence: 27.6 μL of a 6.15 μM solution of *Ct*UGGT$_{GT24}$ were diluted to 1.7 μM with the addition of 71.4 μL of the same buffer. After the spectrum was measured, 1 μL of 5M-8OH-Q 250 mM in DMSO was added and the spectrum measured again. N-NHS-RED-*Ct*UGGT$_{GT24}$ fluorescence: a spectrum was first measured from 99 μL of a 1.7 μM solution of N-NHS-RED-*Ct*UGGT$_{GT24}$; a second spectrum was measured after addition of 1 μL of 5M-8OH-Q 250 mM in DMSO.

Purification of the 2AA-M9 and 2AA-M5-9 *N*-glycans

N-glycans were cleaved from HIV gp120 protein expressed in HEK293F cells in the presence of 5 μM kifunensine,[94] labelled with 2-anthranylic acid (2AA) and purified by HPLC following the protocol in.[42] A 2AA calibration curve was obtained by measuring 2AA fluorescence on a BMG Labtech ClarioSTAR spec, with λ_{excit}=320(15) nm, λ_{emiss}=420(20) nm, for a dilution curve of 2AA in a Greiner 384 wells plate between 730 μM to 273 nM. Using this calibration curve, the concentration of the purified 2AA-Man$_9$GlcNAc$_2$ glycan was estimated as 2 mM and the one of the 2AA-Man$_{5\text{-}9}$GlcNAc$_2$ glycan was estimated as 3 mM.

Estimation of 2AA-Man5-9:*Ct*UGGT$_{GT24}$ K$_d$ by MST and LEF *in vitro*

Measurements were carried out in quartz capillaries on a NanoTemper Monolith X. Initial fluorescence and thermophoresis were measured with λ_{Excit}=650 nm, λ_{Emiss}=670 nm. Each of three independent 16-point dilution series of 2AA-Man$_{5\text{-}9}$GlcNAc$_2$ glycan from 1.5 mM to 45.8 nM was mixed with NT-RED-NHS-labelled *Ct*UGGT$_{GT24}$ 100 nM and a buffer containing NaCl 100 mM, HEPES 20 mM pH 7.4 and 0.05% Tween.

The 2AA-M5-9 glycan : *Ct*UGGT$_{GT24}$ binding was characterised by microscale thermophoresis (MST). The data were fitted with one equilibrium model using the instrument's data analysis software.

The same measurements were repeated with samples made 40 μM 5M-8OH-Q and the binding characterised by LEF (the enhanced NT-RED-NHS-labelled *Ct*UGGT$_{GT24}$ fluorescence once 5M-8OH-Q binds to the labelled protein precludes the use of MST to follow glycan binding in presence of 5M-8OH-Q). The data were analysed by custom-written Python code. A single equilibrium model was used to obtain an apparent dissociation constant, by solving a system of 4x16=64 equations in 3x16+3=51 unknowns. For the ith data point in the 16-points 2AA-M5-9 dilution series, the four equations read:

$$
\begin{aligned}
{}^{app}K_d^L &= \frac{[P]_i * [L]_i}{[P:L]_i} \\
[P]_{tot} &= [P]_i + [P:L]_i \\
[L]_{tot,i} &= [L]_i + [P:L]_i \\
Fluo([P]) &= a * \frac{[P]_i}{[P]_{tot}} + b * \left(1 - \frac{[P]_i}{[P]_{tot}}\right)
\end{aligned}
\qquad \text{(Equation 1)}
$$

where P=NT-RED-NHS-labelled *Ct*UGGT$_{GT24}$ and L=2AA-M5-9.

The 51 variables are the 16x3 values of $[P]_i$, $[L]_i$ and $[PL]_i$ for i=1 to 16, plus a, b and ${}^{app}K_d{}^{2AA\text{-}M5\text{-}9}$. The solution gave ${}^{app}K_d{}^{2AA\text{-}M5\text{-}9}$=341 μM ; a= 605.1 counts; b= 205.6 counts. These values were used in the last equation of the system (1) to compute the fluorescence in the desired interval of $[2AA\text{-}M5\text{-}9]_{tot}$ (blue curve in Figure 4).

The calculated fluorescence curve expected by the two simultaneous and competing equilibria was computed by first solving one system of 5 equations in 5 unknowns for each i-th data point in the dilution series, i=1 to 16:

$$
\begin{aligned}
K_d^{5M-8OH-Q} &= \frac{[P]_i[5M-8OH-Q]_i}{[P:5M-8OH-Q]_i} \\
K_d^{2AA-M5-9} &= \frac{[P]_i[2AA-M5-9]_i}{[P:2AA-M5-9]_i} \\
[P]_{tot} &= [P]_i + [P:5M-8OH-Q]_i + [P:2AA-M5-9]_i \\
[5M-8OH-Q]_{tot} &= [5M-8OH-Q]_i + [P:5M-8OH-Q]_i \\
[2AA-M5-9]_{tot,i} &= [2AA-M5-9]_i + [P:2AA-M5-9]_i
\end{aligned}
\qquad \text{(Equation 2)}
$$

Once the values of $[P]_i$, $[5M\text{-}8OH\text{-}Q]_i$, $[P{:}5M\text{-}8OH\text{-}Q]_i$, $[2AA\text{-}M5\text{-}9]_i$ and $[P{:}2AA\text{-}M5\text{-}9]_i$ were obtained for each of the 16 values of $[2AA\text{-}M5\text{-}9]_{tot,\,i}$, a least-squares fit was carried out to obtain the coefficients A and B from a fit to the experimental data, using the 16 equations in the dilution series, i=1,16:

$$Fluo\left([2AA-M5-9]_{tot,i}\right) = A*\left([P]_i + [P:2AA-M5-9]_i\right) + B*[P:5M-8OH-Q]_i \quad \text{(Equation 3)}$$

The solution gave A = 1,621 counts/μM and B = 11,105 counts/μM. Using these values, the calculated fluorescence curve was computed using Equation 3 for the values of $[2AA\text{-}M5\text{-}9]_{tot}$ in the desired interval (red dashed line in Figure 4).

Estimation of 5M-8OH-Q:*Ct*UGGT$_{GT24}$ K_d by LEF *in vitro*

Measurements were carried out in quartz capillaries on a NanoTemper Monolith X. Fluorescence was measured with λ_{Excit}=650 nm at λ_{Emiss}=670 nm. Each of three independent 16-point dilution series of 5M-8OH-Q from 2.5 mM to 76.3 nM was mixed with NT-RED-NHS-labelled *Ct*UGGT$_{GT24}$ 100 nM and a buffer containing NaCl 100 mM, HEPES 20 mM pH 7.4 and 0.05% Tween. The data were fitted by solving the following system of 4 equations:

$$\begin{aligned} K_d &= \frac{[P]*[L]}{[PL]} \\ [P]_{tot} &= [P] + [PL] \\ [L]_{tot} &= [L] + [PL] \\ Fluo([P]) &= a*\frac{[P]}{[P]_{tot}} + b*\left(1 - \frac{[P]}{[P]_{tot}}\right) \end{aligned} \quad \text{(Equation 4)}$$

in the four unknowns [P], [L], [PL] and K_d, depending on the two parameters a (the maximum observed fluorescence, when all the labelled protein is saturated with inhibitor) and b (the minimum observed fluorescence, when all the labelled protein is free).

The first three equations give the fraction of free protein f_P as a function of the total concentrations of ligand and protein:

$$f_P = \frac{-\left(K_d+[L]_{tot}-[P]_{tot}\right)+\sqrt{\left(K_d+[L]_{tot}-[P]_{tot}\right)^2+4K_d[P]_{tot}}}{2[P]_{tot}} \quad \text{(Equation 5)}$$

and the fourth equation of the system (4) is re-written as:

$$Fluo(f_P) = a*f_P + b(1-f_P) \quad \text{(Equation 6)}$$

The fit to the data was effected by least-squares estimation of the a and b parameters.

Estimation of 2AA-M9:*Ct*UGGT$_{GT24}$ K_d by FPA *in vitro*

Four dilutions series of *Ct*UGGT$_{GT24}$ to in 120 mM NaCl, 20 mM HEPES pH 7.2 (from 247 to 2.47 μM) in a Greiner 384 wells plate were mixed with 2.5 μL of a 2μM solution of 2AA-Man$_9$GlcNAc$_2$ glycan in water, and protein buffer added to a total volume of 25 μL. The final concentration of 2AA-Man$_9$GlcNAc$_2$ glycan was 200 nM.

The anisotropy of the 2AA-fluorescence polarisation was measured on a BMG Labtech ClarioSTAR spectrophotometer, with λ_{excit}=360(15) nm, λ_{emiss}=490(20) nm, and the dichroic mirror set to 410 nm. Both instrument gain coefficients were set to 1,000. The curve was fitted with a single equilibrium constant, and a parameter for minimum value of the anisotropy (the maximum value of the anisotropy was set to 110 mA and kept fixed).

In cellula UGGT-mediated glucosylation assays

The *in cellula* UGGT-mediated glucosylation assays were carried out[47,48] in presence of increasing amounts of 5M-8OH-Q.

Briefly, HEK293-6E cells were plated and grown for 24 hr before replacing with fresh media containing the drug, from a stock solution of 250 mM in 100% DMSO, diluted to the desired/tested concentration (no more than 1% final DMSO in the media).

After a 5 hr incubation time, the media was collected and the adhered cells were removed from the plate with lysis buffer. The media fraction was gently spun down (250 g for 5 min) to collect the dissociated cells and combined with the cells scraped off the plate. The combined samples were then shaken for 10 min at 4°C before being spun at 14,000 g for 10 min at 4°C prior to analyzing the soluble fraction.[47,48]

Fifty μL bed volume of glutathione beads was added to each sample and incubated for 1 hr at 4°C under gentle rotation to remove non-specific protein binding to the resin. The samples were then spun at 1,000 g for 5 min at 4°C to pellet the beads and the supernatant was collected. 20% of the supernatant was used for WCL and 60% was added to the GST-CRT conjugated glutathione beads,[47,48] and incubated

for 16 hr at 4°C under gentle rotation. The beads were collected by centrifuging at 1,000 g for 5 min at 4°C. The supernatant was aspirated and beads were washed twice with lysis buffer without protease inhibitors.

Beads were treated with reducing sample buffer (30 mM Tris-HCl pH 6.8, 9% SDS, 15% glycerol, 0.05% bromophenol blue). WCLs were trichloroacetic acid (TCA) precipitated by adding TCA to cell lysate to a final concentration of 10%. Cell lysate was then briefly rotated and allowed to incubate on ice for 15 min before centrifugation at 17,000 g for 10 min at 4°C. Supernatants were aspirated and washed twice with cold acetone and centrifuged at 17,000 g for 10 min at 4°C. Supernatants were aspirated and the remaining precipitant was allowed to dry for 5 min at room temperature and briefly at 65°C. Precipitated protein was resuspended in sample buffer. Samples were resolved on a 9% reducing SDS-PAGE and imaged by immunoblotting.

Viability assay for treated HEK293-6E cells

The viability of cells after drug treatment was determined using a LUNA II™ Automated Cell Counter. Briefly, untreated and treated cells were incubated with the drug 5 hr. After incubation cells were collected and washed twice with PBS and resuspended in 1 mL of culture media. Cells were mixed with trypan blue (50:50 mix) and viability was measured.

QUANTIFICATION AND STATISTICAL ANALYSIS

The percentage glucosylation was calculated by dividing the normalized amount of protein detected in the GST-calreticulin lane by the normalized total amount of protein in the WCL. This value was then divided by the amount of protein found in the WCL multiplied by 5 to account for the dilution factor and then multiplied by 100. The resulting value yielded the percent reglucosylation in each cell type.

The band intensities were determined using ImageJ v1.53i for pixel quantification. All statistics, biological replicates, and significance information are reported in the figure legends. Prism v8 was used for all quantifications and the error bars were calculated using the standard deviation of three independent biological replicates. Statistical significance was determined by using an unpaired t test with a confidence interval of 95%.